Master's thesis

NTNU
Norwegian University of Science and Technology
Faculty of Engineering
Department of Structural Engineering

Ådne Lund

An experimental and numerical study of welded T-joints between rectangular hollow sections

Master's thesis in Civil and Environmental Engineering
Supervisor: Arild Holm Clausen
June 2020

NTNU
Norwegian University of
Science and Technology

Ådne Lund

An experimental and numerical study of welded T-joints between rectangular hollow sections

Master's thesis in Civil and Environmental Engineering
Supervisor: Arild Holm Clausen
June 2020

Norwegian University of Science and Technology
Faculty of Engineering
Department of Structural Engineering

NTNU
Norwegian University of
Science and Technology

Department of Structural Engineering
Faculty of Engineering
NTNU – Norwegian University of Science and Technology

ACCESSIBILITY

OPEN

MASTER THESIS 2020

SUBJECT AREA:	DATE:	NO. OF PAGES:
Computational Mechanics	30.06.20	10 + 77

TITLE:

An experimental and numerical study of welded T-joints between rectangular hollow sections

En eksperimentell og numerisk studie av sveiste T-knutepunkter av rektangulære hulprofiler

BY:

Ådne Lund

SUMMARY:
The present study examines the behavior of welded T-joints between rectangular hollow section members of similar width. Such joints are used in Vierendeel trusses, moment resisting frames and building diaphragms, where the connections might have significant bending moments from the brace and high axial forces in the chord.

Based on the available literature on RHS T-joints, there seems to be no experimental tests performed on joint under these conditions. In the design recommendations, the chord stress function, Q_f, which is used to account for the reduced moment resistance in the joint due to the presence of an axial force in the chord, is based on experimental results on joints with a brace-width-to-chord-width-ratio of 0.6, which have a different failure mechanism.

To investigate the behavior of such RHS T-joints, experimental tests of eight joints were performed. The experimental tests revealed that the design recommendations in prEN 1993-1-8 are very conservative in predicting the allowed compression force in the chord when the in-plane bending moment from the brace is close to the design moment resistance of the joint. This might indicate that the loads from the brace are transferred to chord in a more efficient manner, thus allowing for higher loads in the brace.

In addition to the experimental testing, a finite element model for predicting the behavior of RHS T-joints of similar width, submitted to an axial compressive load in the chord and an in-plane bending from the brace, was developed. The constructed FE model was calibrated and validated with the new experimental test results and it was shown that the model was able to predict both the deformation pattern and the resistance of the joints.

RESPONSIBLE TEACHER: Arild Holm Clausen

SUPERVISOR(S): Arild Holm Clausen, Panagiotis Manoleas

CARRIED OUT AT: The Department of Structural Engineering, NTNU

Preface

This master thesis represents my final work as a student at the Norwegian University of Science and Technology (NTNU). Furthermore, it symbolizes the end of a 5-year master's degree in Civil and Environmental Engineering with a main profile in computational mechanics.

Having the opportunity to be a part of this research project has given good knowledge about steel joints, mechanics and the practical use of Finite Element Modelling. I consider both the theoretical and practical experience as a privilege and look forward to putting it to use.

I would like to express admiration and gratitude to my supervisors Arild H. Clausen and Panagiotis Manoleas. Thank you for all of the feedback and guidance. Your outstanding knowledge and ability to share your experiences has been vital for this process.

In addition, I would like to thank my family for always having my back and supporting me in my choices. I am very lucky to come from such a safe and supportive environment.

Finally, I want to thank my girlfriend Elisabeth Sagen, for all your love and support. You are incredible and I look forward to moving into our new apartment.

Trondheim, 30th June 2020

Ådne Lund

Abstract

The present study examines the behavior of welded T-joints between rectangular hollow section members of similar width. Such joints are used in Vierendeel trusses, building diaphragms and moment resisting frames, where the connections might have significant bending moments from the brace and high axial forces in the chord.

Based on the available literature on RHS T-joints, there seems to be no experimental tests performed on joint under these conditions. In the design recommendations, the chord stress function, Q_f, which is used to account for the reduced moment resistance in the joint due to the presence of an axial force in the chord, is based on experimental results on joints with a brace-width-to-chord-width ratio of 0.6, which have a different failure mechanism.

To investigate the behavior of such RHS T-joints, experimental tests of eight joints were performed. The experimental tests revealed that the design recommendations in prEN 1993-1-8 are very conservative in predicting the allowed compression force in the chord when the in-plane bending moment from the brace is close to the design moment resistance of the joint. This might indicate that the loads from the brace are transferred to chord in a more efficient manner, thus allowing for higher loads in the brace.

In addition to the experimental testing, a finite element model for predicting the behavior of RHS T-joints of similar width, submitted to an axial compressive load in the chord and an in-plane bending from the brace, was developed. The constructed FE model was calibrated and validated with the new experimental test results and it was shown that the model was able to predict both the deformation pattern and the resistance of the joints.

Sammendrag

I dette studiet blir sveiste T-knutepunkter av rektangulære hulprofiler (RHS) med lik elller nesten lik bredde undersøkt. Slike knutepunkt er brukt i Vierendeelfagverk, bæresystemer i bygninger og momentstive rammer hvor det kan være både betydelige bøyemoment i bjelken og store aksialkrefter i søylen.

Ut i fra tilgjengelig litteratur om RHS T-knutepunkt, virker det som det ikke har blitt gjennomført noen eksperimentelle knutepunktstester under disse forholdene. I beregninsstandarden prEN 1993-1-8, er funksjonen, Q_f, brukt for å ta hensyn til den reduserte momentkapasiteten til knutepunktene når det er en aksialkraft i søylen. Denne er derimot basert på eksperimentelle tester utført på knutepunkt med et forhold mellom bredden på bjelken og søylen på 0.6, hvor det er en annen bruddform.

For å undersøke oppførselen til knutepunktene med bøyemoment i bjelken og aksialkrefter i søylen, ble åtte knutepunktstester gjennomført i laboratorium. Testene viste at formlene i standarden prEN 1993-1-8 er veldig konservative i beregningen av hvor stor aksialkraft man kan ha i søylen når bøyemomentet i bjelken er nær momentkapasiteten til knutepunktet. Dette kan tyde på at kreftene i bjelken blir overført mer effektivt til søylen, slik at det er mulig å ha større laster i bjelken.

I tillegg til de eksperimentell testene ble det også utviklet en FE-modell for å kunne kjøre elementmetodesimuleringer av knutepunktene. FE-modellen ble kalibrert og validert ved hjelp av resultatene fra de eksperimentelle testene og det ble vist at modellen var i stand til å gjenskape både lastkapasiteten og deformasjonen til knutepunktene.

Contents

List of Symbols

t_0	Thickness of the chord wall
t_1	Thickness of the brace wall
b_0	Width of chord wall
b_1	Width of brace wall
b_e	Effective width of cross section
h_0	Height of chord wall
h_1	Height of brace wall
n	Stress ratio in the chord
f_{y0}	Characteristic yield stress of the chord
f_{y1}	Characteristic yield stress of the brace
$f_{0.2}$	0.2% proff stress
f_b	Buckling stress
Cf	Material factor
Q_f	Chord stress function
$M_{ip,Rd}$	Design moment resistance for in-plane bending
$M_{pl,Rd}$	Design plastic moment capacity
W_{pl}	Plastic section modulus
N_{pl}	Axial yield capacity
η	Brace-height-to-chord-width ratio
β	Brace-width-to-chord-width ratio
χ	Reduction factor for buckling
γ_{M5}	Partial safety factor
$\overline{\gamma}$	Normalized slenderness
ε	Parameter used to define section class limitations
ε_1	Longitudinal strain
ε_2	Transverse strain
ε_{el}	True elastic strain
ε_{pl}	True plastic strain

Chapter 1

Introduction

The excellent properties of the tubular shape in structural applications have been well-known for a long time. Structural hollow sections are strong and efficient, providing a high strength to weight ratio which reduces the material usage and allows for greater spans. This generally results in lightweight structures that are aesthetically attractive, long lasting and robust.

Due to their geometric shape, rectangular hollow sections (RHS) have outstanding static strength properties in regard to loading in compression, torsion and bending in all directions. Compared to an open steel section of similar size and area, the radius of gyration about the minor axis is considerably higher, which results in a much lower slenderness ratio for the same effective length and therefore a higher compression capacity. Another benefit is that the resistance against torsion is considerably better for closed sections than for open sections. Furthermore, the rounded corners give a better protection period of coatings against corrosion and because of the closed section shape and the possibility to use smaller members than conventional sections due to their higher structural efficiency, the area which needs to be corrosion protected is smaller (Wardenier et al., 2009).

The most economical and common way to connect RHS members is by welding them directly together without any intersecting plates or gussets. In contrast to circular hollow section joints, there is no need for any specialized profiling, which makes the welding procedure rather straightforward and more economical. RHS T-joints are commonly used in Vierendeel trusses, moment resisting frames and building diaphragms, where the connections

might have significant bending moments from the brace and high axial forces in the chord. In this case, the most common modes of failure for the joint are chord face failure, chord side wall failure and brace failure. An illustration of a RHS T-joint is given in Fig. 1.1.

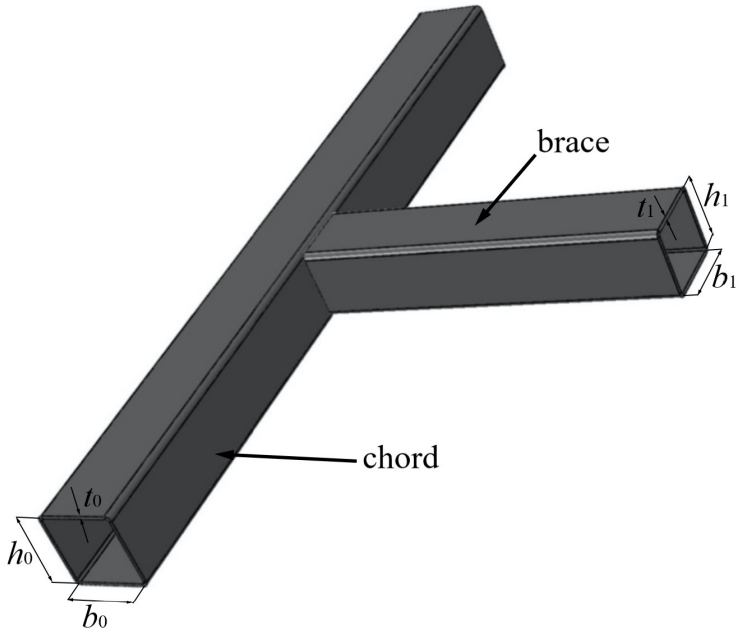

FIGURE 1.1: Illustration of RHS T-joint.

When calculating the joint resistance, the current design rules provide formulas for the different failure modes. In the presence of axial forces in the chord, a chord stress function, Q_f, is used to account for the reduction in moment resistance. However, it might seem like this function is based on experimental test results for brace-width-to-chord-width ratios, $\beta = b_1/b_0$, below 0.85 and then extended to larger β-values with the use of numerical models and analytical equations. Accordingly, the current design equations might be less accurate for joints with β-values between 0.85 and 1.0.

The aim of this master thesis is thus to examine the behavior of welded T-joints consisting of RHS members of similar width, with an axial compressive load in the chord and an in plane bending moment from the brace. As a part of this research, experimental tests of eight RHS T-joints have been performed and based on the experimental results a finite element model, which is fully calibrated and validated with the experimental results, has been developed. Based on the experimental and numerical results as well as the current design rules, recommendations for the design of RHS T-joint submitted

to a combined loading situation are proposed.

Chapter 2

Summary of existing literature

2.1 Introduction

According to Wardenier et al. (2010b), the production of rectangular hollow sections started in 1952, but it was not until 1965 that the first tests were conducted on connections consisting of RHS members. Since then, numerous studies on the behavior of RHS T-joints with brace loading, bending moment or a combination of those have been performed, but the majority of these studies have been focused on either joints loaded with only axial forces or joints predominantly under in-plane bending.

Even though there are some studies on joints with both in-plane bending and axial forces in the chord, these are in general based on experimental results where the β-value is quite low. These results might not be accurate for joints between RHS members of similar width, because when the β-value exceeds 0.85 the expected failure mode changes from chord face failure to chord side wall failure.

In this chapter, the current design rules and the experimental, numerical and analytical research these are based on are summarized briefly. Particular focus is on the research behind the chord stress function, which is used to account for the reduced moment resistance in the joint due to the presence of an axial force in the chord.

2.2 Research work

2.2.1 "State of Art" in 1982

In the work of Wardenier (1982), the "State of Art" in the design of hollow section joints as of 1982 were presented. It was written that some research had been performed on the case of rectangular hollow sections loaded by in-plane moments, but that the results were yet to be systematically summarized and analyzed with actual dimensions and actual mechanical properties. Nevertheless, analytical formulas for the design resistance of joints loaded by in-plane bending moments are presented, which are more or less kept as a foundation as more research on the subject is performed. The formulas for the chord side wall failure and the brace failure were directly related to those for axially loaded joints, while the formula for the chord face failure were based upon the yield line theory. However, no information was provided on how to deal with the interaction between axial loading and bending moments for joints with β-values between 0.85 and 1.0. The design equations were presented as following:

Chord face failure, $\beta \leq 0.85$:

$$M_{\text{ip,Rd}} = f_{\text{y0}} t_0^2 h_1 \left[\frac{1-\beta}{2\eta} + \frac{2}{\sqrt{1-\beta}} + \frac{\eta}{1-\beta} \right] \tag{2.1}$$

Brace failure:

$$M_{\text{ip,Rd}} = f_{\text{y1}} \left[W_{\text{pl,1}} - \left(1 - \frac{b_{\text{eff}}}{b_1} \right) b_0 t_1 (h_1 - t_1) \right] \tag{2.2}$$

Chord side wall failure, $\beta = 1.0$:

$$M_{\text{ip,Rd}} = 0.5 f_{\text{b}} t_0 \left(h_1 + 5t_0 \right)^2 \tag{2.3}$$

where:

$\eta = \dfrac{b_0}{2t_0}$, is the half-width-to-thickness ratio of the chord,

$\beta = \dfrac{b_1}{b_0}$, is the brace-width-to-chord-width ratio,

$b_{\text{eff}} = \left(\frac{10.8}{b_0/t_0}\right)\left(\frac{f_{y0}t_0}{f_{y1}t_1}\right) b_1$, is the effective width,

$f_b = \chi f_{y0}$, is the buckling stress with χ being the reduction factor for flexural buckling according to the ECCS buckling curve "a".

2.2.2 Moment connections between RHS (Packer, 1993)

In a paper by Packer (1993), it was written that based on tests recording the maximum joint moment, it was found that this moment typically occurs at excessively large joint deformations. It was thus concluded that for practical design, the moment capacity of a joint could be determined similarly as for RHS T-joints with an axial load in the brace. A chord stress function was introduced based on the research by de Koning and Wardenier (de Koning & Wardenier, referred in Packer, 1993, p.67), but it is only valid for the chord face failure. This function is presented as:

$$f(n) = 1.2 + \frac{0.5}{\beta} n \leq 1.0 \tag{2.4}$$

where:

$n = \frac{N_0}{A_0 f_{y0}} < 0$, is the chord stress parameter.

In the case of a chord side wall failure, it is written that tests have shown that buckling is less critical for moment loaded T-joints than axially loaded T-joints (de Koning & Wardenier, referred in Packer, 1993, p. 69). Consequently, it is determined that when calculating the design moment resistance for chord side wall failure, the chord yield stress, f_{y0}, is used instead of the buckling stress, f_b.

2.2.3 The Static Strength of Uniplanar and Multiplanar Connections in Rectangular Hollow Sections, (Yu, 1997)

In 1988 an ECSC (European Community of Steel and Coal) research program was launched, which consisted of experimental tests of uniplanar X- and T-joint and multiplanar XX-, TX- and KK-joints with a fixed β-value of 0.6. As part of a PhD research program aimed towards providing design recommendations on the static strength of uniplanar and multiplanar connections in

rectangular hollow sections by Yu (1997), the experimental results from the ESCS research program were presented and a numerical model was developed and calibrated against the numerical results. The calibrated numerical model was then used for an extensive parameter study and based upon the experimental and numerical results as well as the analytical formulas provided by Wardenier in 1982, new design recommendations for the static strength of connections in RHS sections were proposed. The effect of an axial force in the chord was however not taken into account.

2.2.4 Background of the chord stress function

In the 3rd edition of the "IIW Static Design Procedure for Welded Hollow Section Joints" (2009), the up to date design recommendations for RHS joints as of 2009 were presented. These recommendations were in accordance with the "CIDECT design guide for RHS joints under predominantly static loading" (2009) and the background of the new RHS joint strength equations were provided in a paper by Wardenier et al. (2010a).

The most significant addition was the new chord stress function which was included to account for the effect on the joint strength in the case of axial forces and bending moments in the chord. This function was the result of work based on RHS by Yu (1997), where the FE-model was based on experimental results on joints with β = 0.6, and further analyses of his work in the CIDECT programs 5BK and 5BU. The accuracy of the chord stress function was then assessed by comparison with available FE-data by Wardenier et. al (2007a), to get a chord stress function which was consistent for both RHS and CHS joints. Consequently, it would seem like the chord stress function and the resulting design equations for joints with larger β-values came from FE-data based on experiments with β = 0.6, which again were compared against the analytical formulas. The chord stress function takes the form:

$$Q_f = (1 - |n|)^{C_1} \tag{2.5}$$

where:

$n = \dfrac{N_{0,Ed}}{A_0 f_{y0}} + \dfrac{M_{ip,0,Ed}}{W_{ip,pl,0} f_{y0}}$, is the chord stress parameter,

$C_1 = 0.6 - 0.5\beta$, is a joint parameter depending on the β-value.

2.2.5 Current design guidance

The current version of the Eurocode, EN 1993-1-8 (2009), does not contain the updated design recommendations as recommended by CIDECT and IIW. However, in the internal work document prEN 1993-1-8 (2018), the proposed changes to the Eurocode were presented with up to date design recommendations, which included the chord stress function from the CIDECT and IIW recommendations. As opposed to these recommendations, the buckling stress is used for the chord side wall failure instead of the design yield stress, and in addition a material factor C_f was included to account for higher yield stresses. This document is however still not public, and it is possible that changes can be introduced. The design equations for the relevant failure modes in EN 1993-1-8 and prEN 1993-1-8 were presented as following:

EN 1993-1-8

Chord face failure, $\beta \leq 0.85$:

$$M_{\mathrm{ip,Rd}} = k_{\mathrm{n}} f_{\mathrm{y0}} t_0^2 h_1 \left[\frac{1}{2\eta} + \frac{2}{\sqrt{1-\beta}} + \frac{\eta}{1-\beta} \right] \frac{1}{\gamma_{\mathrm{M5}}} \tag{2.6}$$

Brace failure, $0.85 \leq \beta \leq 1.0$:

$$M_{\mathrm{ip,Rd}} = f_{\mathrm{y1}} \left[W_{\mathrm{pl,1}} - \left(1 - \frac{b_{\mathrm{eff}}}{b_1} \right) b_1 t_1 h_1) \right] \frac{1}{\gamma_{\mathrm{M5}}} \tag{2.7}$$

Chord side wall failure, $\beta = 1.0$:

$$M_{\mathrm{ip,Rd}} = 0.5 f_{\mathrm{y0}} t_0 \left(h_1 + 5t_0 \right)^2 \frac{1}{\gamma_{\mathrm{M5}}} \tag{2.8}$$

where:

$k_{\mathrm{n}} = \begin{cases} 1.3 - \dfrac{0.4n}{\beta} \leq 1.0 & \text{for } n > 0 \text{ (compression)} \\ 1.0 & \text{for } n \leq 0 \text{ (tension)} \end{cases}$, is a chord stress function,

$b_{\text{eff}} = \left(\frac{10}{b_0/t_0}\right)\left(\frac{f_{y0}t_0}{f_{y1}t_1}\right) b_1 \leq b_1$, is the effective width.

prEN 1993-1-8

Chord face failure, $\beta \leq 0.85$:

$$M_{\text{ip,Rd}} = C_f f_{y0} t_0^2 h_1 \frac{Q_f}{\gamma_{M5}} \left[\frac{1}{2\eta} + \frac{2}{\sqrt{1-\beta}} + \frac{\eta}{1-\beta}\right] \tag{2.9}$$

Brace failure:

$$M_{\text{ip,Rd}} = f_{y1} C_f \left[W_{\text{pl},1} - \left(1 - \frac{b_{\text{eff}}}{b_1}\right) b_1 t_1 (h_1 - t_1)\right] \tag{2.10}$$

Chord side wall failure, $\beta = 1.0$:

$$M_{\text{ip,Rd}} = 0.5 C_f f_b t_0 \frac{Q_f}{\gamma_{M5}} (h_1 + 5t_0)^2 \tag{2.11}$$

where:

$C_f = \begin{cases} 1.0 & \text{for } f_y \leq 355 \\ 0.9 & \text{for } 355 < f_y \leq 460 \\ 0.8 & \text{for } 460 < f_y \leq 700 \end{cases}$, is a material factor depending on the yield strength[1],

$f_b = \chi f_{y0}$, is the critical buckling stress with χ being the reduction factor for flexural buckling obtained from EN 1993-1-1.

For values of β between 0.85 and 1.0, the design resistance should be calculated with the help of a linear interpolation between the governing resistances at $\beta = 0.85$ (chord face failure and brace failure) and the governing resistances at β = 1.0 (chord side wall failure and brace failure). The design process is illustrated in Fig. 2.1.

[1] If the yield strength exceed $0.8 f_u$, the design yield strength should be taken as $0.8 f_u$

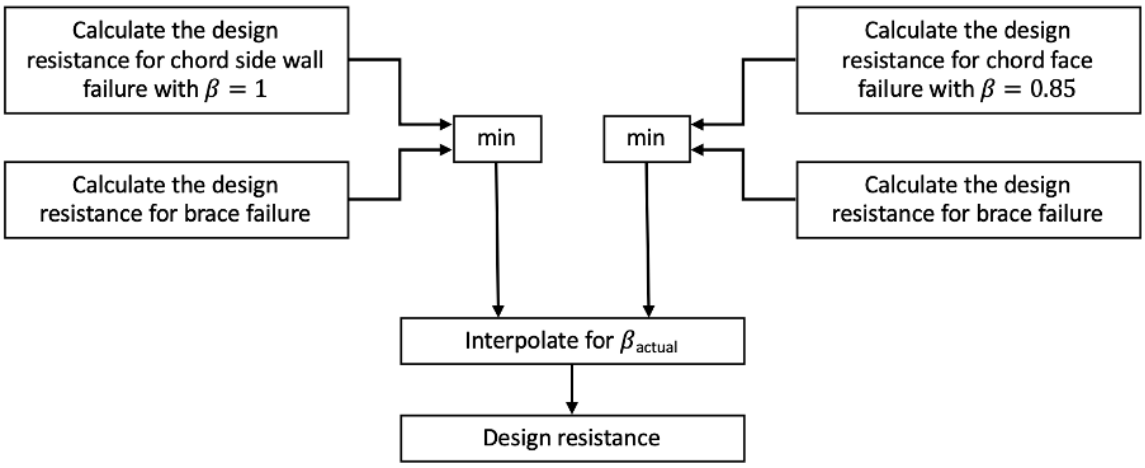

FIGURE 2.1: Illustration of the process for finding the design resistance in the case of a β-value between 0.85 and 1.0.

Chapter 3

Design and setup of the experimental work

3.1 Introduction

Based on the available literature on RHS T-joints, there seems to be no experimental tests performed on RHS T-joints of similar width subjected to a combined load situation with a compression force in the chord and an in-plane bending moment coming from the brace. To properly investigate the behavior of RHS T-joints under such conditions, it was therefore decided to perform eight joint tests in the laboratory of the Department of Structural Engineering at NTNU.

3.2 Configuration of the joints

3.2.1 Selection of RHS profiles

Due to limitations in the usable height and compression capacity of the test rig, it was decided to use $100\times100\times4$, $100\times100\times3$ and $90\times90\times4$ RHS profiles of S355 structural steel. These profiles were only available in the cold formed catalogue, which introduces some complications compared to the use of hot-rolled specimens. During the cold forming process, the sections undergo plastic deformation, which results in enhanced strength, a corresponding loss of ductility, residual stresses and typically non-homogeneity

of the material properties around the section. In particular, the corner regions have to sustain a high level of cold work, which according to Hancock et al. (2005), lead to an average increase in the yield stress about 1.22 times higher than for the flat faces.

3.2.2 Joint configuration

The RHS T-joints were produced by welding the RHS members directly together. Rectangular hollow sections can in general be joined with fillet welds, but in the case of equal or near-equal widths, a partial butt weld on the side walls, as shown in Fig. 3.1, is necessary to ensure a good connection. To ensure sufficient deformation capacity, the welds should be designed to give a resistance that is not less than the brace member capacity, which for fillet welds results in a throat thickness a > 1.10 t, for steel grade S355 (Wardenier et al., 2009).

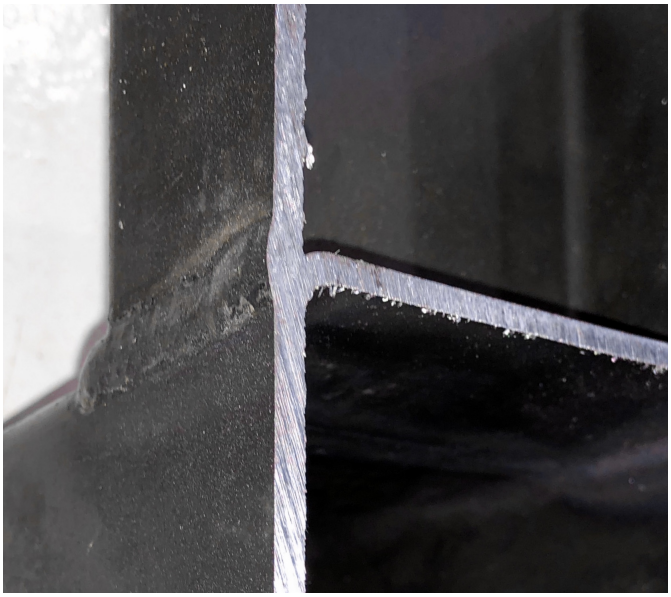

FIGURE 3.1: Cut through the welded connection in specimen C1B10M70, showing the partial butt weld used to connect two RHS profiles of equal width.

In total, eight RHS T-joints were produced by the workshop Trondheim Stål with properties as listed in Table 3.1. The name, CxBxxMxx, is based on the column class, with Cx denoting the column class, Bxx denoting the beta value and Mxx denoting the applied moment as a percentage of the in-plane moment resistance of the joint. Since the profiles for the first two specimens, C1B10M70 and C1B09M90, were ordered a couple months earlier than the

rest of the profiles, they came from a different batch. To distinguish between the different profiles, A- is added as a prefix to the first batch and B- is added as a prefix to the second batch. The cross-sectional properties of the profiles are listed in Table 3.2.

TABLE 3.1: Joint properties.

	Chord	Brace	l_{chord} [mm]	l_{brace} [mm]	Chord class	β	$\frac{M_{ip,Ed}}{M_{ip,Rd}}$
C1B10M70	A-100×4	A-100×4	1000	381	1	1.0	0.7
C1B10M90	B-100×4	B-100×4	698	381	1	1.0	0.9
C1B09M70	B-100×4	B-90×4	698	381	1	0.9	0.7
C1B09M90	A-100×4	A-90×4	1000	381	1	0.9	0.9
C2B10M70	B-100×3	B-100×4	698	381	2	1.0	0.7
C2B10M90	B-100×3	B-100×4	698	381	2	1.0	0.9
C2B09M70	B-100×3	B-90×4	698	381	2	0.9	0.7
C2B09M90	B-100×3	B-90×4	698	381	2	0.9	0.9

TABLE 3.2: Cross-sectional properties of the profiles.

RHS profile	Measured thickness, t [mm]	Area, A [mm^2]	Moment of inertia, I [mm$^4\times 10^6$]	Plastic section modulus, W_{pl} [mm$^3\times 10^3$]
A-100×4	3.73	1401	2.13	50.11
A-90×4	4.7	1547	1.84	48.84
B-100×4	4.08	1523	2.30	54.23
B-100×3	2.96	1123	1.74	40.58
B-90×4	3.84	1285	1.57	41.11

3.2.3 In-plane bending moment

To introduce an in-plane bending moment to the joint, it was decided to attach a dead load to the end of the brace. Consequently, it is ensured that the load is applied vertically downwards and kept constant over time. Steel plates with weight corresponding to either 70 or 90 % of the in-plane moment resistance were hung from the end of the brace with a steel rod. The steel rod was attached to a triangular steel plate, welded to two 120 mm×120 mm steel plates with 20 mm thickness, which was welded to the end of the RHS member. The final configuration of the joint is shown in Fig. 3.2.

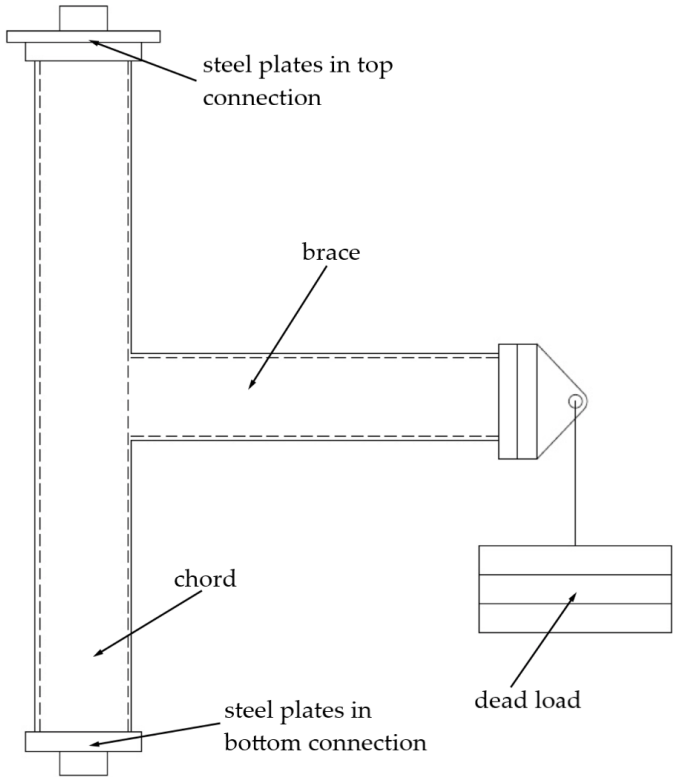

FIGURE 3.2: Configuration of the RHS T-joint for the experimental work.

3.3 Design resistance

The design resistance of the specimens is calculated in accordance with the design recommendations of the Eurocodes. The relevant design checks are found in EN 1993-1-1 (2015), which is used to calculate the resistance of the chord, and EN 1993-1-8 (2009) and prEN 1993-1-8 (2018), which are used to calculate the resistance of the joint.

As described in Section 3.2, the RHS profiles were selected such that the chord was in class 1 or 2. However, this selection was based on the nominal material properties, which were found to be significantly lower than the actual values found in the material test, which is presented in Chapter 4. As a result of this, the profiles which were supposed to be in class 2, ended up being in class 4, meaning that plastic design is not allowed and that the formulas for calculating the moment resistance of the joint are outside the validity range.

In reality, this is not a unique problem. The characteristic yield strength of steel is usually defined as the value of yield stress below which not more than five percent of the test values may be expected to fall, which means that this strength is expected to be exceeded by 95 % of the cases (Gambhir, M. L., 2013). Although a deviation between the nominal and actual material properties might be expected, this raises an issue with how to perform the calculations of the specimens. In agreement with my supervisors, it was decided to go with two cases; using the measured geometric and material values without the safety factor γ_M, and using the nominal values with the suggested safety factors. The calculations based on the measured values were used to determine the design value of the bending moment in the brace.

3.3.1 Design resistance of the chord

The cross-sectional resistance of the chord is calculated according to the design recommendations in EN 1993-1-1. As described in Section 3.2, three different RHS profiles were used. To identify the extent to which the resistance and rotation capacity of the cross section is limited by its local buckling resistance, the chord is classified according to the width-to-thickness ratio and the material parameter $\varepsilon = \sqrt{235/f_y}$. Using this classification, the chords are classified as listed in Table 3.3.

TABLE 3.3: Classification.

RHS profile	Nominal	Measured
A-100×4	Class 1	Class 1
B-100×4	Class 1	Class 1
B-100×3	Class 2	Class 4

While the profiles in class 1 and 2 can be designed with plastic design, a profile in class 4 is expected to experience local buckling before the yield stress is reached. Thus, to account for the reduced resistance due to the effects of local buckling, effective section properties may be used. The formulas for calculating the effective area is given in EN 1993-1-5 (2019), and requires an iterative calculation in which the stress ratio, ψ, is determined at each step from the stresses calculated on the effective cross section defined at the end of the previous step. Since the design value of the bending moment, $M_{y,Ed}$, is different for each of the specimens, the stress distribution is different as well, such that the effective section properties are different between the specimens. However, as can be seen in Table 3.4, it was found that this difference was very low.

TABLE 3.4: Effective section properties.

	Effective area, A_{eff}	Effective moment of inertia, I_{eff}	Effective section modulus, W_{eff}
C2B10M70	$1033\,mm^2$	$1.62\,mm^4 \times 10^6$	$31.00\,mm^3 \times 10^3$
C2B10M90	$1034\,mm^2$	$1.62\,mm^4 \times 10^6$	$31.00\,mm^3 \times 10^3$
C2B09M70	$1035\,mm^2$	$1.62\,mm^4 \times 10^6$	$31.01\,mm^3 \times 10^3$
C2B09M90	$1036\,mm^2$	$1.62\,mm^4 \times 10^6$	$31.01\,mm^3 \times 10^3$

For a class 4 cross section under bending and axial force the following criterion should be met:

$$\frac{N_{Ed}}{A_{c,eff}} + \frac{M_{y,Ed} + N_{Ed} e_{Ny}}{W_{eff,y,min}} \leq \frac{f_y}{\gamma_{M0}} \tag{3.1}$$

where:

$W_{eff,y,min}$, is the effective section modulus of the cross section,

e_{Ny}, is the shift of the relevant centroidal axis when the cross-section is subjected to compression only,

$\gamma_{M0} = 1.05$, is a partial factor.

while for the profiles in class 1 and 2, the interaction formula for calculating the reduced moment resistance under the presence of an axial load is given as:

$$M_{\mathrm{N,Rd}} = M_{\mathrm{pl,Rd}} \frac{1-n}{1-0.5a_{\mathrm{w}}} \leq M_{\mathrm{pl,Rd}} \tag{3.2}$$

where:

$M_{\mathrm{pl,Rd}} = \dfrac{W_{\mathrm{pl}} f_{\mathrm{y}}}{\gamma_{\mathrm{M0}}}$, is the plastic moment resistance,

$n = \dfrac{N_{\mathrm{Ed}}}{N_{\mathrm{Rd}}}$,

$a_{\mathrm{w}} = \dfrac{A-2bt}{A} \leq 0.5$

By setting the design value of the bending moment, $M_{\mathrm{y,Ed}}$, equal to 70 or 90 % of the joint moment resistance, $M_{\mathrm{ip,Rd}}$, the formulas can be rewritten to calculate the reduced compression resistance in the presence of a constant bending moment. Since the value of the joint moment resistance is dependent on the properties of both the chord and the brace, the compression resistance needs to be calculated for each of the specimens. The results are listed in Table 3.5.

TABLE 3.5: Compression resistance of the chord.

	$M_{\mathrm{y,Ed}} = 0.7M_{\mathrm{ip,Rd}}$		$M_{\mathrm{y,Ed}} = 0.9M_{\mathrm{ip,Rd}}$	
	$N_{\mathrm{M,Rd,nom}}$	$N_{\mathrm{M,Rd,real}}$	$N_{\mathrm{M,Rd,nom}}$	$N_{\mathrm{M,Rd,real}}$
C1B10Mxx	465.6 kN	618.7 kN	454.3 kN	782.1 kN
C1B09Mxx	464.2 kN	783.1 kN	452.4 kN	600.1 kN
C2B10Mxx	367.9 kN	532.7 kN	362.8 kN	526.5 kN
C2B09Mxx	364.1 kN	521.3 kN	358.0 kN	511.5 kN

3.3.2 Design resistance of the joint

As described in Chapter 2, the current version of the Eurocode, EN 1993-1-8, does not contain the updated design recommendations as recommended by

CIDECT and IIW. The up to date design recommendations are however provided in the proposed update to EN 1993-1-8, prEN 1993-1-8. The main difference between these design guides is the chord stress function, Q_f, and the material factor, C_f, which are not included in EN 1993-1-8. The design formulas from the prEN 1993-1-8 are rewritten here for convenience.

Chord face failure, $\beta \leq 0.85$:

$$M_{ip,Rd} = C_f f_{y0} t_0^2 h_1 1 \frac{Q_f}{\gamma_{M5}} \left[\frac{1}{2\eta} + \frac{2}{\sqrt{1-\beta}} + \frac{\eta}{1-\beta} \right] \tag{3.3}$$

Brace failure:

$$M_{ip,Rd} = f_{y1} C_f \left[W_{pl,1} - \left(1 - \frac{b_{eff}}{b_1} \right) b_1 t_1 (h_1 - t_1) \right] \tag{3.4}$$

Chord side wall failure, $\beta = 1.0$:

$$M_{ip,Rd} = 0.5 C_f f_b t_0 \frac{Q_f}{\gamma_{M5}} (h_1 + 5t_0)^2 \tag{3.5}$$

As opposed to the design recommendations in EN 1993-1-1, where the resistance of the chord could be calculated for the class 4 profiles by using the effective section properties, there is no guidance on how to deal with profiles in class 3 or 4 in neither EN 1993-1-8 or prEN 1993-1-8. Since the class 4 sections is outside of the scope of the design recommendations, and since plastic design is not allowed, it was therefore decided to use the effective area and the effective section modulus in this case.

For the specimens with $\beta = 1$, the relevant design checks are for brace failure and chord side wall failure, while the specimens with $\beta = 0.9$ are designed with the help of a linear interpolation between the governing resistances at $\beta = 0.85$ and the governing resistances at $\beta = 1.0$, as illustrated in Fig. 2.1. The resulting moment resistances are listed in Table 3.6, where $M_{ip,Rd,nom}$ is calculated using the nominal values and $M_{ip,Rd,real}$ is calculated using the measured geometric and material values.

TABLE 3.6: Joint moment resistance.

	EN 1993-1-8		prEN 1993-1-8	
	$M_{\text{ip,Rd,nom}}$	$M_{\text{ip,Rd,real}}$	$M_{\text{ip,Rd,nom}}$	$M_{\text{ip,Rd,real}}$
C1B10M70	10.22 kNm	12.21 kNm	5.28 kNm	4.34 kNm
C1B10M90	10.22 kNm	16.18 kNm	5.28 kNm	5.23 kNm
C1B09M70	8.59 kNm	13.60 kNm	5.47 kNm	6.59 kNm
C1B09M90	8.59 kNm	10.24 kNm	5.47 kNm	5.31 kNm
C2B10M70	7.04 kNm	10.51 kNm	2.41 kNm	2.02 kNm
C2B10M90	7.04 kNm	10.51 kNm	2.41 kNm	2.02 kNm
C2B09M70	5.87 kNm	8.76 kNm	2.92 kNm	3.22 kNm
C2B09M90	5.87 kNm	8.76 kNm	2.92 kNm	3.22 kNm

With the joint moment resistance known, the allowed compression force in the chord can be deduced from the chord stress function, Q_{f}. However, since the EN 1993-1-8 does not account for an axial force in the chord, this is only possible for the prEN 1993-1-8 recommendations. By calculating the n-value corresponding to the desired moment resistance of 70 or 90 % of the joint moment resistance and rewriting the formula for the chord stress function as shown in Eq. (3.6), the joint compression resistance can then be calculated. The resulting joint compression resistances are listed in Table 3.7

$$N_{\text{M,rd}} = A f_{\text{y}} \left(n - \frac{M_{\text{ip,Ed}}}{W_{\text{pl}} f_{\text{y}}} \right) \tag{3.6}$$

TABLE 3.7: Allowed compression in the chord with a constant bending moment, M_{Ed}.

	M_{Ed}	$N_{M,rd,nom}$	$N_{M,Rd,real}$
C1B10M70	3.04 kNm	462.9 kN	589.3 kN
C1B10M90	4.71 kNm	278.3 kN	475.3 kN
C1B09M70	4.62 kNm	406.9 kN	658.2 kN
C1B09M90	4.78 kNm	170.3 kN	227.0 kN
C2B10M70	1.41 kNm	369.5 kN	492.4 kN
C2B10M90	1.82 kNm	233.2 kN	301.3 kN
C2B09M70	2.26 kNm	323.3 kN	409.9 kN
C2B09M90	2.90 kNm	146.3 kN	155.6 kN

3.4 Rig setup

In the initial phase of the design of the joints, it was considered which boundary conditions were most favorable not only for the laboratory setup, but also for design of the numerical model. In the case of clamped boundary conditions, both the general setup and the numerical modelling is fairly straightforward, but possible problems might be introduced because it in general is very difficult to ensure that the connections are actually clamped. Another alternative would be to use a pinned connection, which could be done e.g. with the use of a ball joint. However, there is a possibility of introducing some friction, which can be very difficult to model numerically. The initial choice was therefore to select, clamped boundary conditions in order to simplify the numerical modelling.

3.4.1 First setup

The setup for the first specimen is shown in Fig. 3.3. In an attempt to get clamped boundary conditions, 120×120 mm steel plates with 20 mm thickness were welded to the top and bottom of the chord and secured with two M16 bolts to the base plate in the bottom and the load plate in the top. The

bottom connection is shown in detail in Fig. 3.3b. It can be assumed that for the bottom connection, this was sufficient to achieve an approximately clamped connection, but the same could not be said for the top connection. Since the head of the test-rig was not fixed, there was no lateral stability, such that the movement to the side was not constrained. In an attempt to rectify this problem, a total of four ratchet straps were tied around the head of the test-rig and secured in the surrounding columns as shown in Fig. 3.3a.

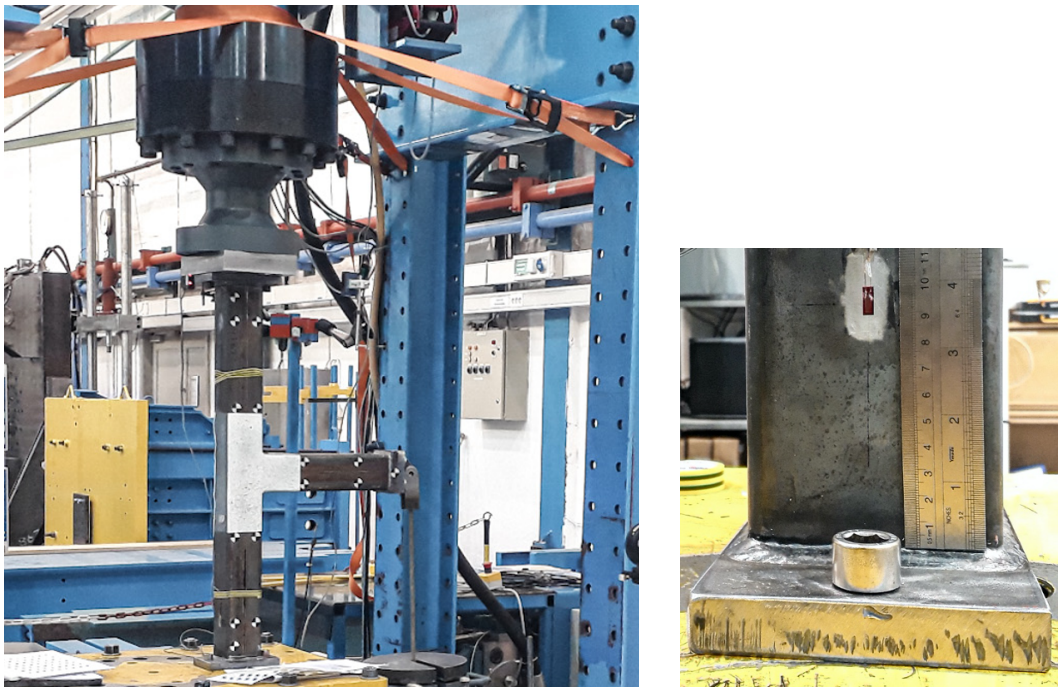

(a) (b)

FIGURE 3.3: a)First setup with ratchet straps, b) Bottom connection in the first setup.

Despite the uncertainty regarding the lateral stability, the first specimen, C1B10M70, was tested with the setup as described. However, it turned out that the ratchet straps had very limited effect and there was in reality almost no lateral stability. As a result, the column head started drifting sideways, resulting in an eccentricity and an extra moment at the connections, which ultimately resulted in the introduction of plastic hinges and unwanted failure of the specimen.

3.4.2 Second setup

Based on the outcome of the first experimental test, it was decided to change the boundary conditions from a clamped to a pinned connection and replace the ratchet straps with a much stiffer setup, with braces made of steel rods. In

the bottom of the specimen, an approximately pinned connection was created by welding an additional 50 mm × 50 mm steel plate with 25 mm thickness beneath the 120 mm × 120 mm steel plate. The 50 mm × 50 mm plate was connected to the base plate by placing the head of an M16 bolt into a cavity in the plate, as shown in Fig. 3.7. In contrast to the alternative with a ball joint which was considered initially, this did not create a perfect hinge. However, because the stress distribution is equal over the surface of the block, this should be satisfactory for the experimental work.

(a) (b)

FIGURE 3.4: Bottom connection in the second setup.

In a new attempt to achieve lateral stability in the top connection, an additional steel plate of 12 mm thickness was placed between the 120 mm × 120 mm steel plate and the 50 mm × 50 mm steel plate which was connected to the load cell, and four steel rods were bolted to this additional plate and connected to rollers in each of the four columns in the test rig. The plate at the top of the chord and the plate in which the steel rods were bolted, were connected to the load cell with two M16 bolts to prevent sideways movement between the plates. The second setup, the top connection and the roller connection are shown in detail in Figs. 3.5 and 3.6.

3.4.3 Testing procedure

With the selected boundary conditions, the specimens were placed in the test-rig, which had a compressive capacity of 2 MN and a maximum usable height of about 1.1 m. As described, the in-plane bending moment was introduced by hanging steel plates with weight corresponding to either 70 or 90 % of the in-plane moment resistance from the end of the brace with a steel rod. In an effort to avoid applying the entire weight to the specimen at once, the steel plates were placed on a fork lifter and gradually lowered.

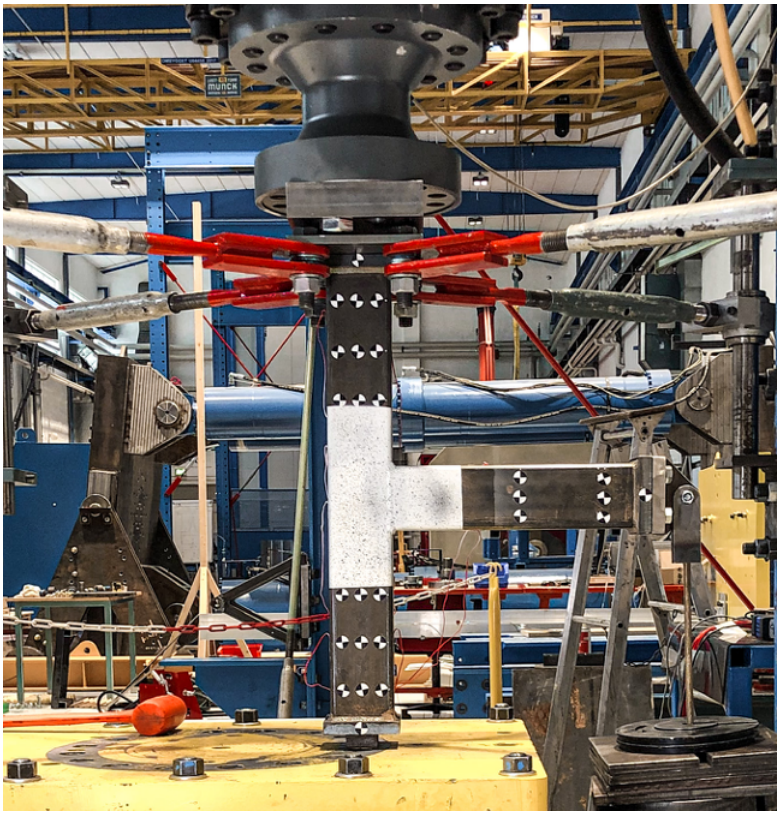

FIGURE 3.5: Second setup with a pinned connection and steel rods for lateral stability.

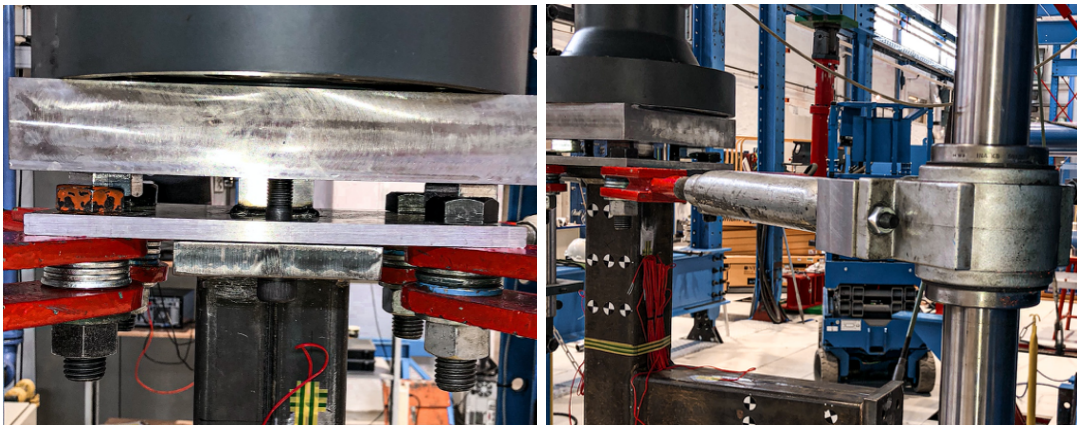

(a) (b)

FIGURE 3.6: a) Top connection in the second setup, b) Roller connection.

Due to the concerns with the introduction of unintended moments on the specimen, great care was taken to align and center the specimen, the different end plates and the head of the test-rig. With the specimen in position, the compressive load in the chord and the dead load in the brace could be applied. This was done in three stages:

- An initial compression load of about 50 kN was applied to stabilize and keep the specimen in place before any moment from the brace was introduced.
- A dead load corresponding to either 70 or 90 % of the in-plane moment resistance of the joint was applied to the end of the brace.
- The compressive load in the chord was gradually increased until failure in the specimen occurred.

3.5 Instrumentation

3.5.1 Digital image correlation (DIC)

DIC is an optically based technique used to obtain full-field coordinates and displacements from a sequence of digital images. The program eCorr was used to perform the correlation, in which the user defined region of interest in an image of a specimen at a deformed stage is compared against an image of the specimen in a reference stage by solving an optimization problem. A fundamental assumption in the DIC measurements is that the pattern on the surface of the specimen follows the deformation of the underlying specimen, so that the images taken throughout the test can be correlated to produce full-field coordinates which is representative of the shape, motion and deformation of the underlying specimen (International Digital Image Correlation Society, 2018).

The regions of interest for the DIC were marked on the specimens, as shown in Fig. 3.7a, with either checkerboard stickers or a black and white speckle pattern, which were sprayed directly on the surface of the specimen.

The area with the speckle pattern was located such that the local buckling behavior of the specimen could be observed. Consequently, 3D coordinate measurements are necessary, which means that a minimum of two cameras, situated at a stereo angle to perform both 3D photogrammetry and image correlation, were required. Before measurements for the 3D-DIC can be performed, the camera system needs to be calibrated with the use of calibration targets of known separation length. This allows the DIC software to correct for lens distortions and provides the location and orientation of the cameras in space with respect to each other and the specimen. In eCorr, a cylinder-based calibration was utilized with a standardized ⌀80 mm cylinder with a

coarse checkerboard pattern. The resulting camera calibration mesh is shown in Fig. 3.8.

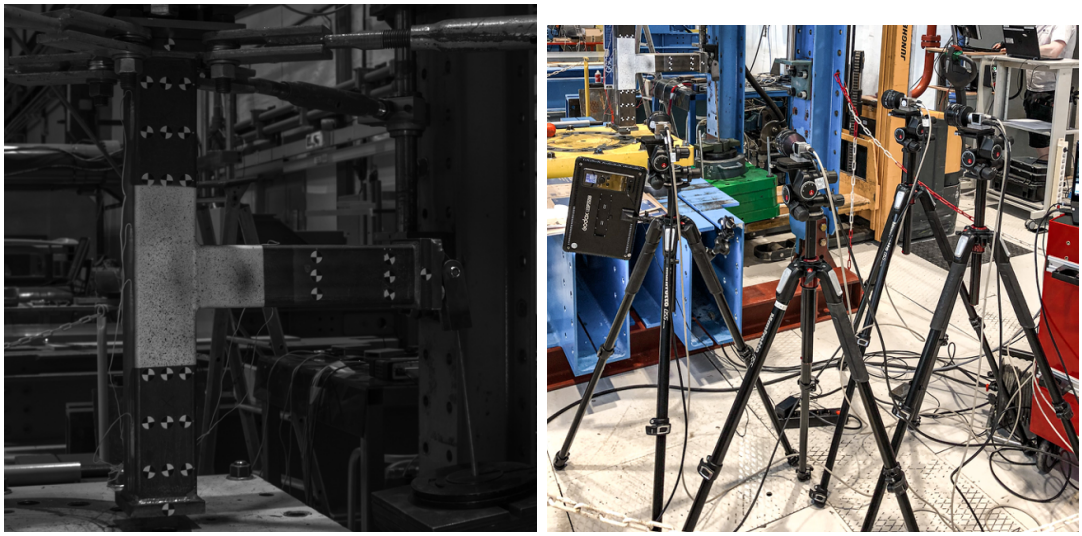

(a) (b)

FIGURE 3.7: a) Regions of interest for the DIC, b) Camera setup.

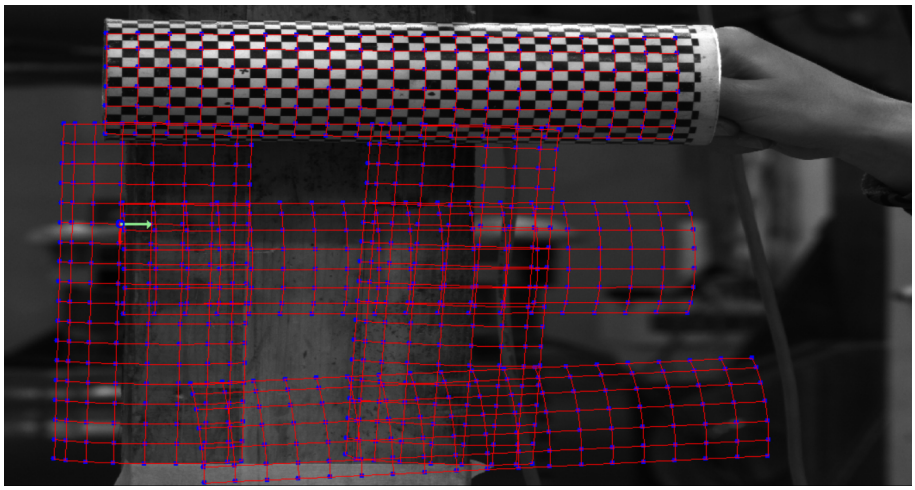

FIGURE 3.8: Calibration mesh obtained from the images of the cylinder calibration targets.

It was planned to do subset 3D-DIC, but since this was not facilitated by eCorr, the average value from the two global cameras was used. Consequently, only the 2D coordinates was measured and not the out-of-plane motion. However, the error associated with out-of-plane motion in 2D-DIC can be reduced by placing the camera far from the specimen, so this should not introduce a significant error (Wang et al., 2017). The positions of the subsets

for the specimens C1B10M70 and C1B10M90 are shown in Fig. 3.9a[1] and the position of the subsets for the other specimens are shown in Fig. 3.9b.

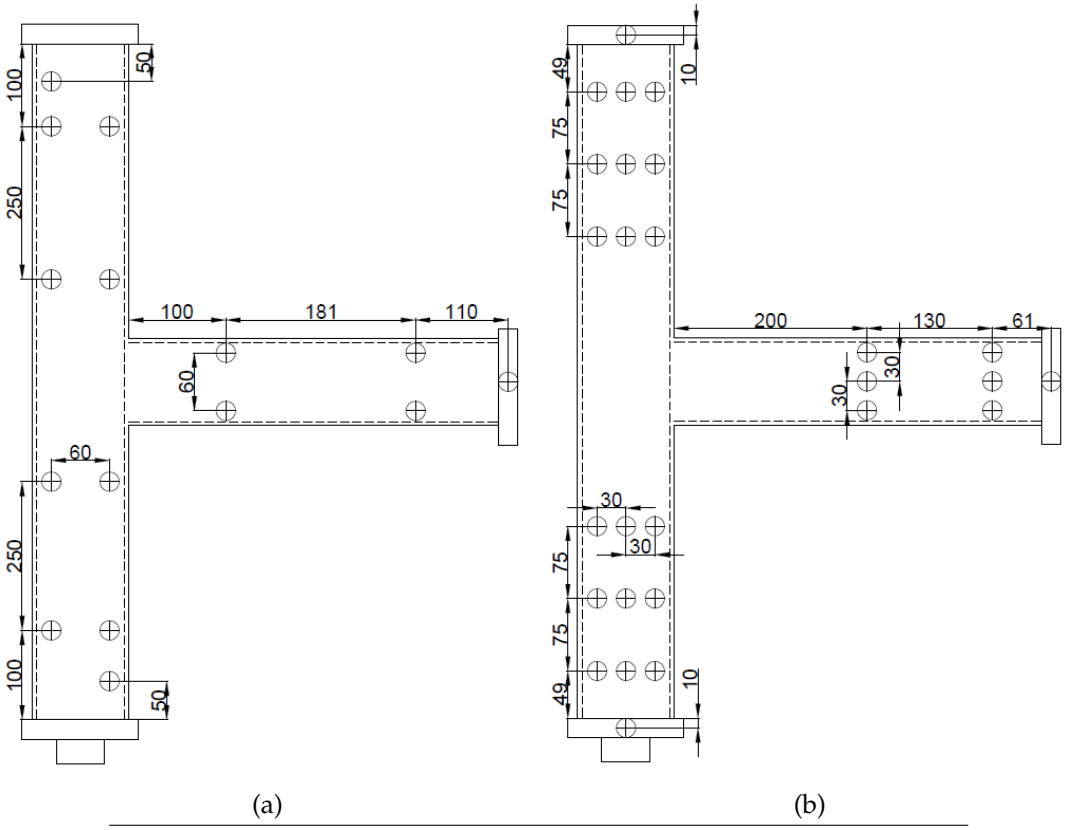

FIGURE 3.9: a) Sticker positions for C1B10M70 and C1B09M90, b) Sticker positions for the other six specimens.

3.5.2 Strain gauges

In addition to the DIC, strain gauges were used to measure the strain at the locations indicated in Fig. 3.10. All gauges were of the type FLA-6-11, which is a 6 mm linear gauge with mild steel compensation.

[1]The bottom sticker in C1B10M70 was placed on the left side

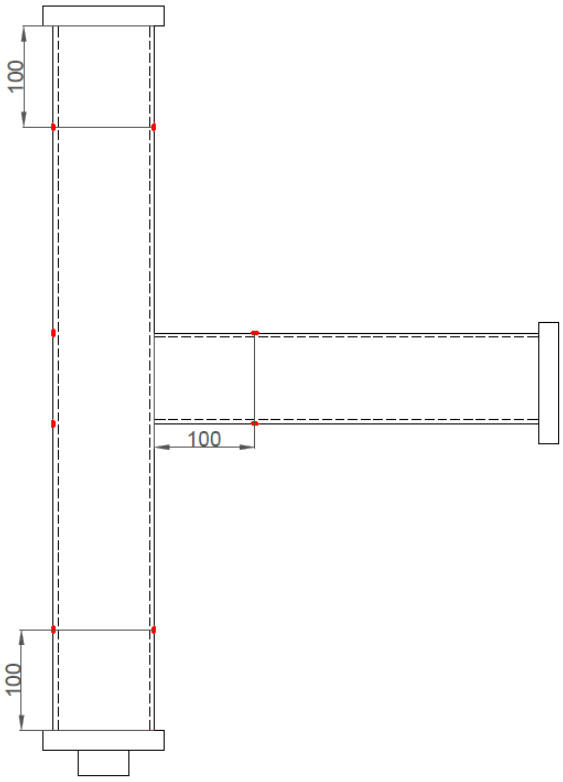

FIGURE 3.10: Position of the strain gauges indicated in red.

Chapter 4

Material test

4.1 Introduction

Tensile tests were performed to determine the mechanical behavior of the material in the joints. The mechanical properties of interest were the yield stress, the true stress-strain relationship and the plastic deformation.

As mentioned in Chapter 3, the first two specimens were ordered a couple months earlier than the rest of the specimens and consequently, the RHS profiles used to construct the specimens came from two different batches. The material test specimens from the first batch were analyzed with DIC, while the specimens from the second batch were analyzed with the help of extensometers.

Compared to the standard method with the extensometer, DIC has the advantage that it can provide the diffuse necking and the local strain as well as the point-by-point strain field (Wang et al., 2010). The fundamental assumption of the extensometer is that the deformation is homogeneous between the two knives of the extensometer, meaning that only the average strain within the gauge length is measured. This means that for the extensometer, the data obtained are only valid up until the onset of diffuse necking, since the deformations are no longer uniform after this point. However, this should not be of concern for the experimental work because the strain at failure for the specimens is expected to be well below the necking strain.

4.2 Setup and experimental procedure

To be able to investigate the material of the specimens, spare parts from the RHS profiles used in the specimens were obtained for the material testing. Unfortunately, there was some trouble with the delivery of the first batch and it later turned out that the spare parts for the 100x100x4 profile came from a different batch than that of the ones used to construct the two first specimens. Consequently, four additional coupons were cut from the specimen, C1B10M70, after it had been tested and analyzed together with the second batch. To minimize the effects of the plastic strain from the testing, the coupons were taken from regions close to the neutral bending axis as shown in Fig. 4.1, where the stresses were minimum.

FIGURE 4.1: Regions in C1B10M70 from which the coupons were cut.

In addition to the four coupons from C1B10M70, three coupons were cut from each of the spare parts, which were corresponding to the profiles used in the specimens. To avoid the area effected by the welding, the side with the longitudinal weld was avoided. The coupons were then machined into standard dimensions as shown in Fig. 4.2.

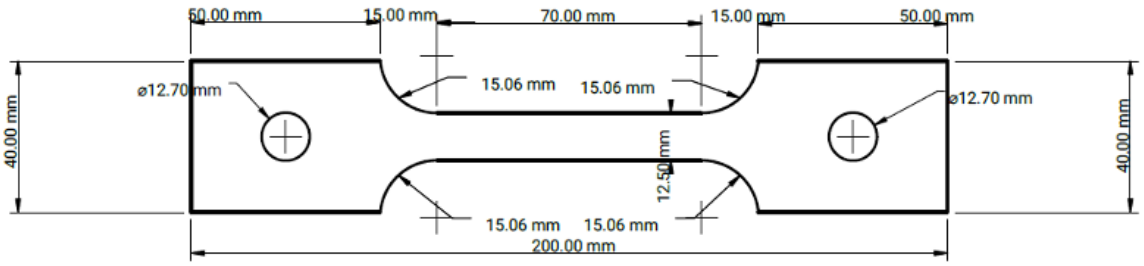

FIGURE 4.2: Coupon dimensions.

The coupons that were cut had a significant curvature, as can be seen in Fig. 4.3. This is most likely a result of residual stresses in the material due to the cold forming process. In a study by Li et al. (2009), it was found that aside from residual stresses on the welding line, the transverse residual stresses were typically below 30 % of the yield stress of the material, while longitudinal residual stresses were slightly higher, but typically below 40 % of the yield stress.

FIGURE 4.3: Visible curvature of coupon.

Because of the curvature of the coupons, an initial stiffness error is introduced as the load is applied and the coupons are straightened out. To correct for this, extensometers were placed on both faces of the coupons and averaged, while for the coupons tested with DIC, this error was corrected during the post processing.

The thickness and the width in the reduced section of the coupons were measured with an electronic digital caliper. The measured values are listed in Table 4.1. To be able to identify which face of the profile the coupons were cut from, the numbers 1, 2 and 3 were added as a suffix, with number 2 representing the face opposite to the weld and number 1 and 3 the adjacent faces. However, the coupons from the A-90 $\times$ 4 were not marked before testing, so

it could not be confirmed from which sides they were cut. In addition, an exception from the identification system was done for the coupons cut from C1B10M70, where number 1, 2 and 3 were taken from the opposite face and number 4 from the adjacent face.

TABLE 4.1: Coupon dimensions.

Coupon	Thickness [mm]	Width [mm]	Cross sectional area [mm^2]
A-100×4-1	3.61	12.42	44.84
A-100×4-2	3.60	12.42	44.71
A-100×4-3	3.56	12.42	44.22
A-100×4-4	3.52	12.41	43.68
A-90×4-1	4.59	12.50	57.38
A-90×4-2	4.62	12.50	57.35
A-90×4-3	4.61	12.50	57.63
B-100×4-1	3.94	12.39	48.82
B-100×4-2	3.92	12.38	48.53
B-100×4-3	3.93	12.39	48.69
B-100×3-1	2.82	12.38	34.91
B-100×3-2	2.82	12.39	34.94
B-100×3-3	2.82	12.39	34.94
B-90×4-1	3.69	12.38	45.68
B-90×4-2	3.66	12.40	45.38
B-90×4-3	3.71	12.39	45.97

Because of issues with access to the lab during the Corona lock down, the second batch were tested by SINTEF, where a Zwick testing machine was utilized, while the first batch was tested in the NTNU laboratory with an Instron testing machine. However, the setup and procedure were similar for both the batches, with the coupons attached to the testing machine with a pin, as shown in Fig. 4.4, and a constant rate of displacement set at 2.1 mm per minute. Since this deformation is measured as the displacement of the piston stroke, which is not accurate enough for the calculation of the strains,

extensometers or DIC were utilized to make sure proper readings for the strains were obtained.

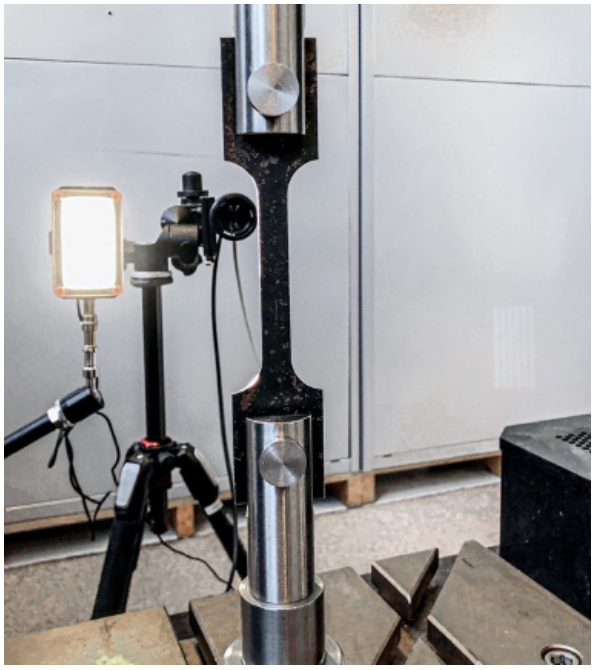

FIGURE 4.4: Setup for tensile tests with DIC.

4.3 Analysis and results

In the first series of material tests, DIC was used to analyze the results. With the use of the program eCorr, a region of interest defined as a structured mesh of 15×15 pixels were generated in the reduced cross section of the coupons. The longitudinal and transverse true strain values could then be obtained directly, by defining vectors spanning over the necking region as shown in Fig. 4.5, while the strain through the thickness was assumed to be equal to the transverse strain.

As opposed to the analysis with DIC, only the longitudinal strain is measured with the extensometers, and the obtained results need to be transformed from nominal strain values to true strain values. The longitudinal strain values were obtained by dividing the elongation of the extensometer by the initial length of the extensometer and taking the average value of the two extensometers. The longitudinal true strain is then found by transforming the nominal strain with the equation:

$$\varepsilon_{\text{true}} = \ln(1 + \varepsilon_{\text{nom}}) \tag{4.1}$$

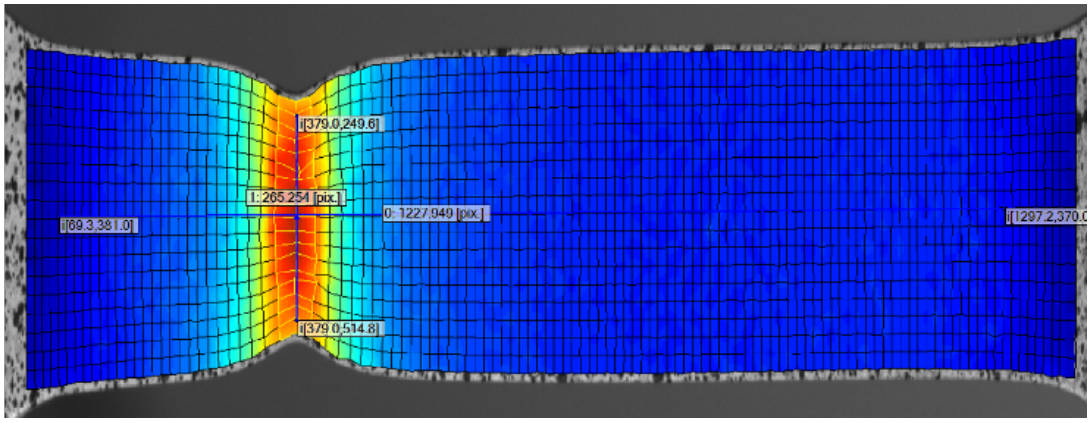

FIGURE 4.5: Mesh and vectors used for measuring the true strain in the DIC.

The strain through the thickness was assumed to be equal to the transverse strain. For the elastic part of the curve, this means that the transverse strain is equal to the longitudinal true strain times the negative Poisson's ratio. For the plastic deformation it is assumed that the material is approximately incompressible, which implies that the volume does not change as the material undergo plastic deformation. This means that the sum of the strains in all three directions need to be equal to zero, which in this case is equivalent to a linear elastic material with a Poisson's ratio of 0.5.

The force data was recorded by the testing machines and automatically synchronized to match the pictures in the DIC or the recordings from the extensometers. With the true strain found, the true stress could then be calculated as:

$$\sigma_{\text{true}} = \frac{F}{A} \tag{4.2}$$

where:

F, is the recorded force,

$A = b \times \varepsilon_{2,\text{true}} \times h \times \varepsilon_{3,\text{true}}$, is the actual cross sectional area.

To correct for the initial error due to the fitting/straightening of the coupons analyzed with DIC, a linear regression was performed in the region between 150-300 MPa. Because the material behavior in this region is linear elastic, it could then be used to extrapolate the region below. However, it should be

noted that the Young's modulus obtained from both the DIC and the extensometers is not totally correct, since this requires a different approach than a tensile test. To obtain proper readings for the Young's modulus, multiple cycles of loading and unloading with loads below the point of yield should be performed. This was deemed unnecessary in this case, since the main objective was to determine the yielding and the onset of plasticity. The resulting true stress-strain curves are shown in Fig. 4.6.

As can be seen in the figure, there are some difference between the coupons both for the yield point and the tensile strength. This can most likely be ascribed to the cold forming process. According to Hancock et al. (2005), the face opposite to the weld is subject to more bending than the adjacent faces in the forming process. Consequently, the yield stress in the opposite faces have been found to be higher than in the adjacent faces, with an average difference ratio of about 1.09 for the yield stress and 1.06 for the tensile strength.

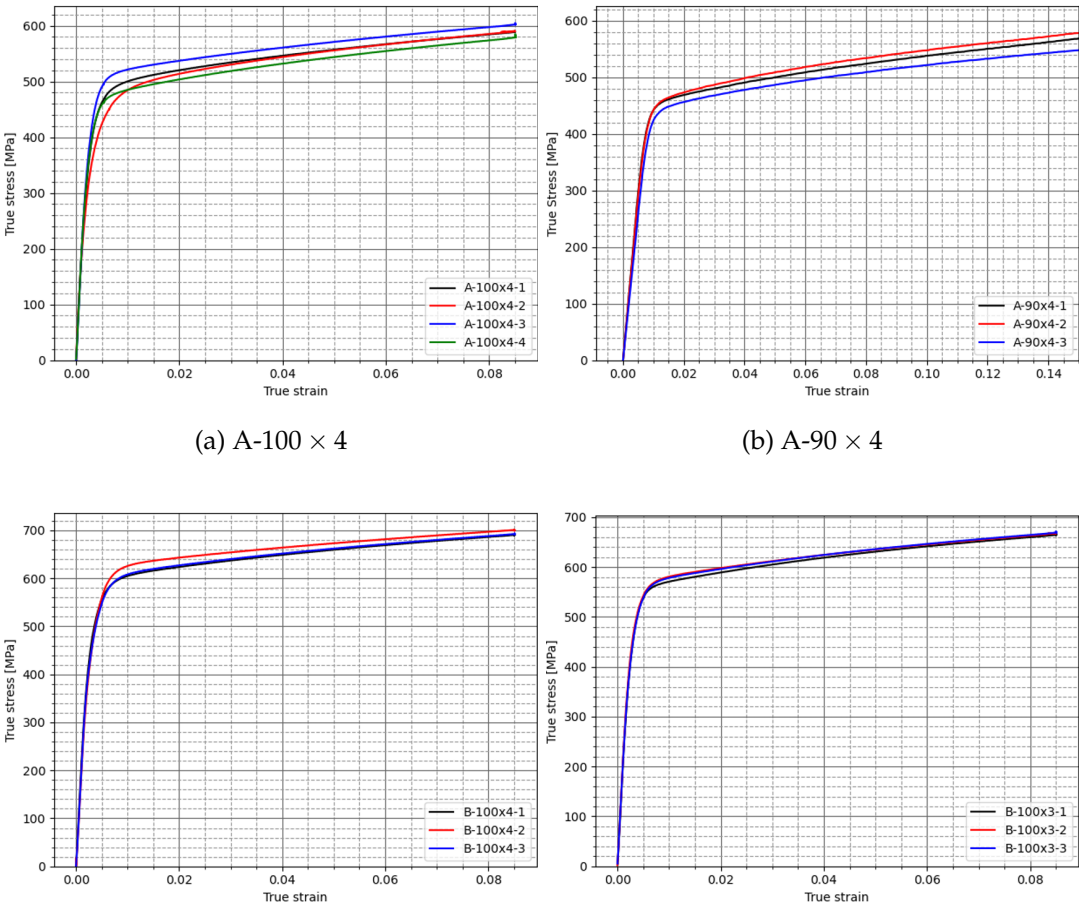

(a) A-100 × 4

(b) A-90 × 4

(c) B-100 × 4

(d) B-100 × 3

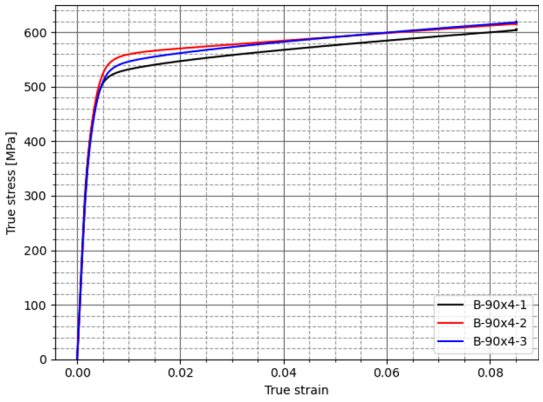

(e) B-90 × 4

FIGURE 4.6: True stress-strain curves of the coupons.

For the weld face, a report by the European Commission (2005) found that the influence of the cold forming on the strength properties did not deviate significantly from the opposite and the adjacent faces. It is thus assumed that the weld face has similar characteristics as the average of the two adjacent faces and the opposite face.

Another consequence of the cold forming process is that there is no yield plateau in the stress-strain curve, such that the 0.2 % proof stress needs to be used as an approximation to the yield stress. This value is found at the intersection between the stress-strain curve and the 0.2 % strain offset of the elastic part of the stress-strain curve as shown in Fig. 4.7.

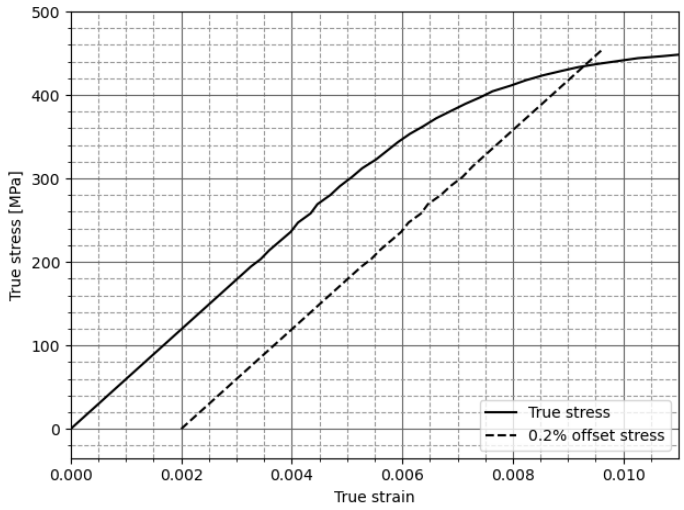

FIGURE 4.7: Method for finding the 0.2 % proof stress.

To account for the differences between the different faces when calculating the 0.2 % proof stress, the ultimate tensile strength and the stress-strain curves for the profiles, the average value over the three sides was taken. The resulting proof stress and ultimate tensile strength are listed in Table 4.2.

TABLE 4.2: Proof stress and ultimate tensile strength.

RHS profile	0.2 % proof stress, $f_{0.2}$	Ultimate tensile strength, f_u
A-100×4	465 MPa	541 MPa
A-90×4	433 MPa	500 MPa
B-100×4	547 MPa	638 MPa
B-100×3	539 MPa	614 MPa
B-90×4	507 MPa	564 MPa

The post-yield behavior of the material is modelled in Abaqus by defining data points with the true stress and the true plastic strain, where the plastic strain is calculated as:

$$\varepsilon_{pl} = \varepsilon_t - \varepsilon_{el} \tag{4.3}$$

where:

ε_t, is the true total strain,

$\varepsilon_{el} = \frac{\sigma_{true}}{E}$, is the true elastic strain.

The values for the true stress were then interpolated for specific strain values for each of the coupons, so that the data from the different coupons could be combined. A plastic data curve with the true stress and the true plastic strain, could then be obtained for each of the profiles by taking the average value of the coupons, as shown in Fig. 4.8 [1].

[1]Since only one of the four coupons from the A-100×100×4 profile came from the adjacent face, a weighted average was used to have the same weight ratio as the other profiles

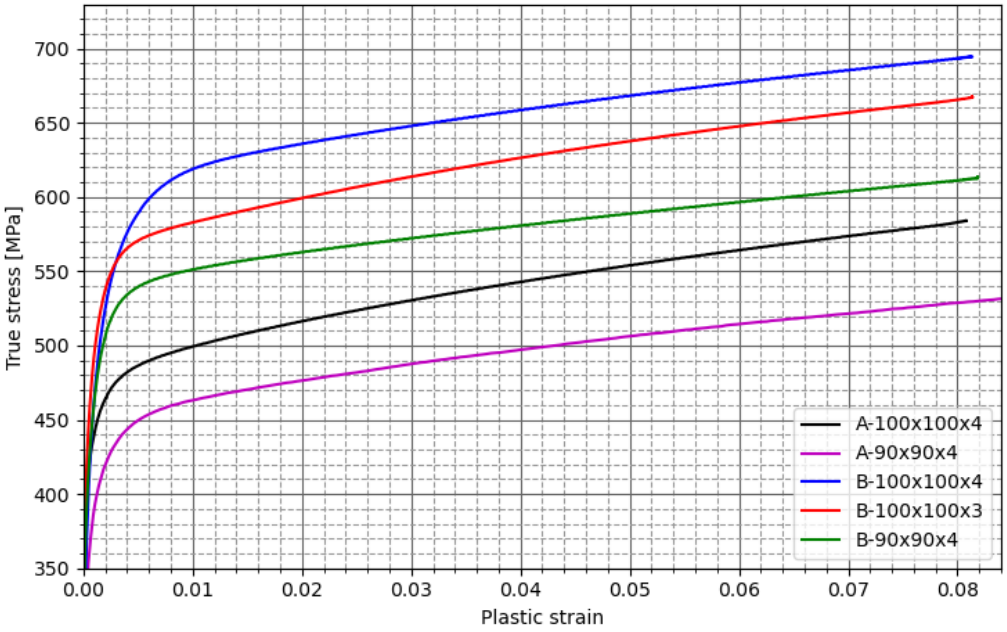

FIGURE 4.8: Plastic curves for the RHS profiles.

As described previously, the cold forming process has a significant effect on the material properties of the different faces. As can be seen in Figs. 4.9a and 4.9b, there is a visible difference between the opposite and the adjacent faces[2]. It was therefore decided to use different values for the adjacent and the opposite face, to be able to accurately model the material behavior in Abaqus.

[2]Since the coupons from the A-90×90×4 profile was not marked, it was assumed that the coupon with the highest yield stress came from the opposite face

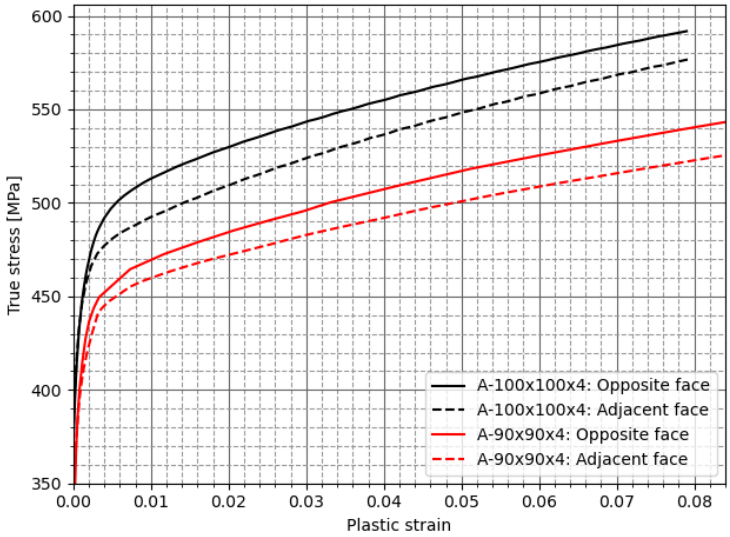

(a)

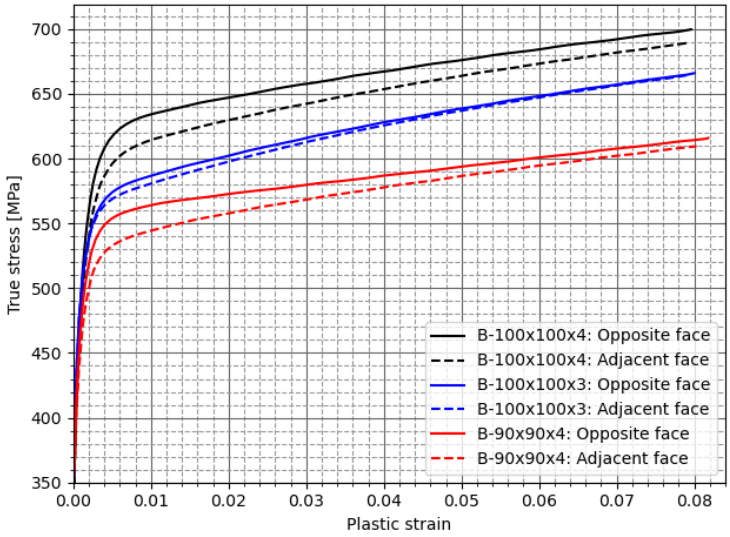

(b)

FIGURE 4.9: Plastic curves for the RHS profiles showing the difference between the adjacent and opposite face of the profiles.

Chapter 5

Tests on joints

5.1 Introduction

The specifications of the specimens, the general setup, the experimental procedure and the design resistance, calculated in accordance with the Eurocodes, were described in Chapter 3. In this chapter, the results for each of the joints is presented, including any deviations from the test procedure and the observed mechanism of failure, and then the results is compared and evaluated against the current design recommendations.

5.2 Test results

5.2.1 C1B10M70

The first specimen which was tested, C1B10M70, had a dead load of 609 kg attached to the end of the brace, which resulted in an in-plane bending moment of about 3.06 kNm. The boundary conditions were fixed, with the use of ratchet straps tied around the head of the test-rig to prevent lateral movement. However, the ratchet straps turned out to be ineffective in securing the lateral stability, which resulted in sideways movement.

In addition, a safety limit was reached when the compressive force in the chord was at 102 kN, most likely because the limit for the maximum stroke was set too low. This resulted in a sudden unloading of the compression

load on the chord. After adjusting the position of the specimen, the test was restarted without removing the dead load in the end of the beam.

After the repositioning of the specimen, it once again started drifting to the side, both in-plane and out-of-plane, as the load was being reapplied. The resulting eccentricity introduced an extra moment at the top and bottom connections, which ultimately resulted in unwanted failure close to the boundary conditions. The in-plane horizontal movement of the top of the chord is illustrated in Fig. 5.1. Because sideways movement at the bottom connection was not fully restricted, the horizontal displacement at the top of the chord was measured relative to the movement at the bottom of the chord.

Despite the lack of lateral stability, the predicted compression resistance in the chord according to prEN 1993-1-8 was exceeded, with the ultimate compression load at failure being almost 627 kN. It is however probable that an even higher load could have been achieved, if not for the issues with the lateral stability.

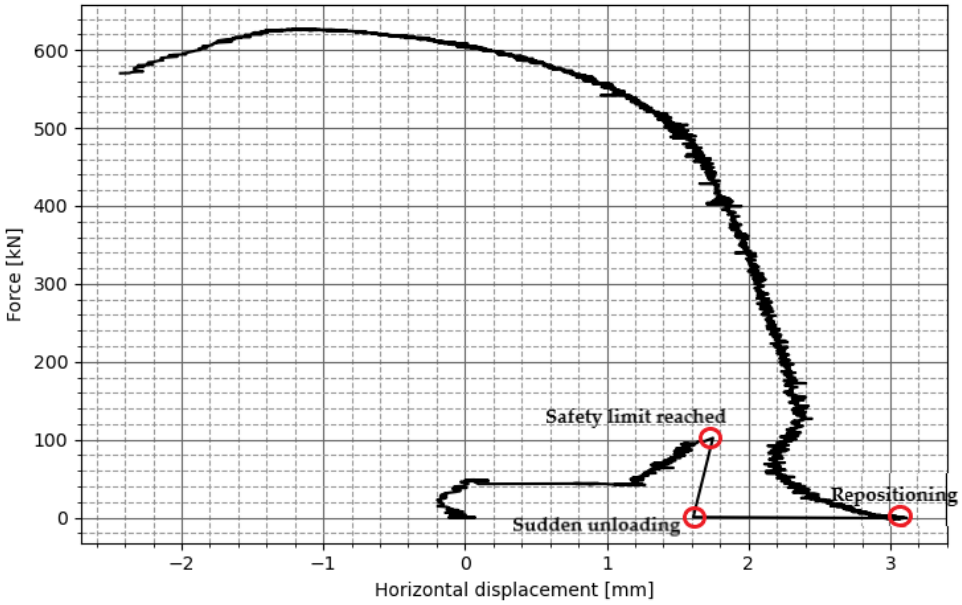

FIGURE 5.1: Force vs. relative in-plane horizontal displacement between the top and the bottom of the chord for specimen C1B10M70.

5.2.2 C1B09M90

Based on the outcome in the testing of the first specimen, it was decided to change the setup of the rig for the second test. As described in Section 3.4.2, the boundary conditions were therefore changed from a fixed to a pinned connection and the ratchet straps were replaced with steel rods. As can be seen in Fig. 5.2, the in-plane horizontal movement of the top of the chord is significantly smaller, which indicates that the steel rods were effective in providing lateral stability.

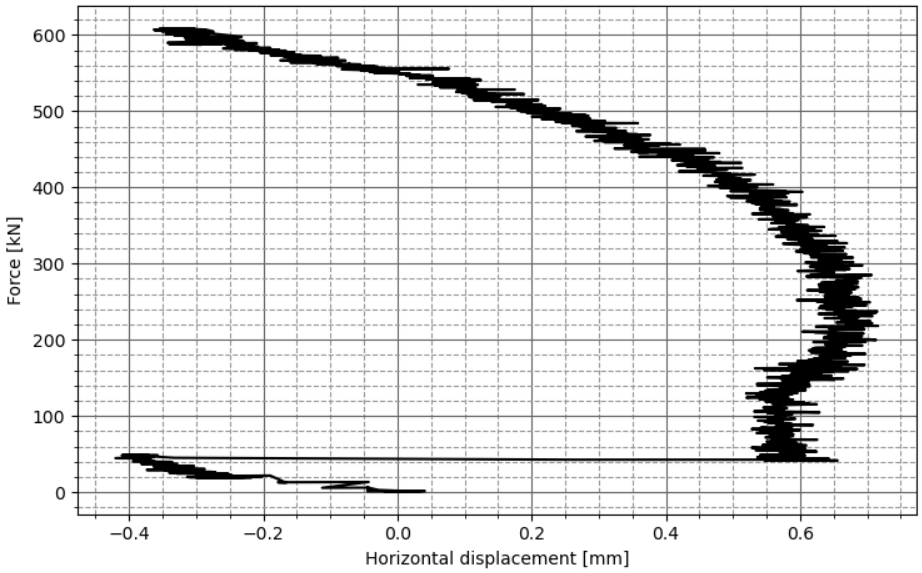

FIGURE 5.2: Force vs. relative in-plane horizontal displacement between the top and the bottom of the chord for specimen C1B09M90.

The dead load in the brace resulted in an in-plane bending moment of about 4.40 kNm, which is quite close to the calculated joint moment resistance. According to the prEN 1993-1-8 predictions, the allowed compression resistance in the chord should drop significantly when the in-plane bending moment comes close to the joint moment resistance. However, this behavior was not observed in the test, with the ultimate compression load at failure reaching about 608 kN. As can be seen in Fig. 5.3, the mechanism of failure is chord side wall failure due to plastic buckling.

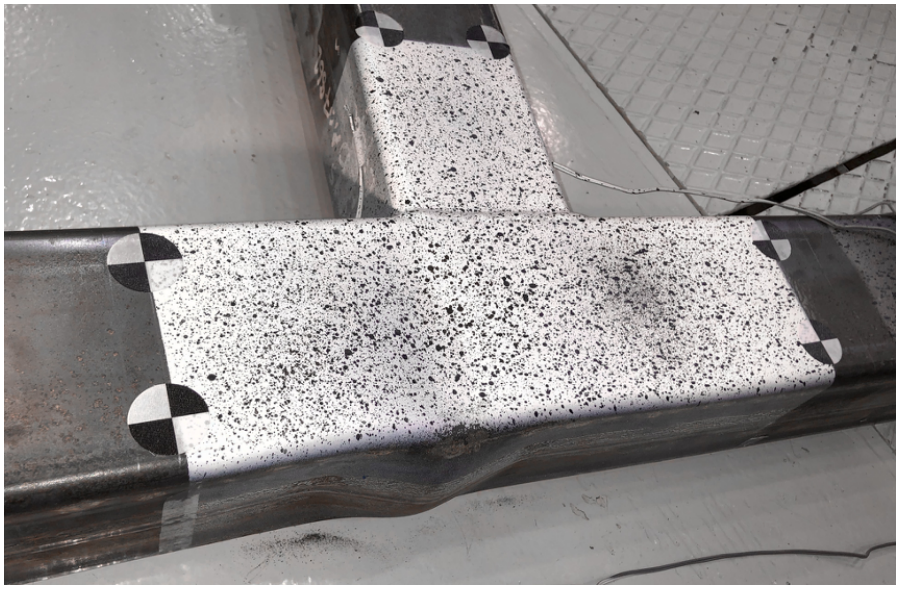

FIGURE 5.3: Visible plastic buckling in the chord side wall for specimen C1B09M90.

5.2.3 C1B10M90

Because of the successful test of C1B09M90, it was decided to keep the second rig setup for the remaining specimens. The specimen C1B10M90, had a dead load of 948 kg attached to the end of the brace, which should have given an in-plane bending moment of about 4.76 kNm. However, as the test was being carried out, it was discovered that one of the plates in the dead load was in contact with the base plate which the specimen was standing on. This contact might have led to less force being transferred to the specimen and in addition, the horizontal force component might contribute in pulling the specimen to the side. The contact is shown in detail in Fig. 5.4.

By looking at the readings from the strain gauges which were attached to the brace, it was possible to perform a check of how much of the dead load was being transferred to the specimen with the formula:

$$M_{\mathrm{ip,E}} = E\varepsilon W_{\mathrm{el}} \tag{5.1}$$

where:

E, is the Young's modulus,

ε, is the recorded strain,

FIGURE 5.4: The green plate in the bottom was in contact with the yellow base plate for specimen C1B10M90.

$W_{el} = \dfrac{I_y}{z_{max}}$, is the elastic section modulus.

Based on Eq. (5.1), it was found that the actual in-plane bending moment was approximately 0.26 kNm less than the intended value. However, by using the same formula to evaluate the other specimens, where the dead load was not in contact with the base plate, it was found that there is a significant measurement uncertainty in the readings from the strain gauges. For this reason, it was not possible to make any certain conclusion about the actual size of the in-plane bending moment. However, by looking at the in-plane horizontal movement of the top of the chord, it is apparent that compared to the other specimens which were tested with the second rig setup, C1B10M90 has a larger relative horizontal displacement which keeps increasing through the loading.

As can be seen in Fig. 5.5, the horizontal displacement at failure is about 4.6 mm. In spite of this, the ultimate compression load was significantly higher than the one predicted by the prEN 1993-1-8, reaching almost 869 kN, and the mechanism of failure was similar to the one observed in C1B09M90 with chord side wall failure due to plastic buckling.

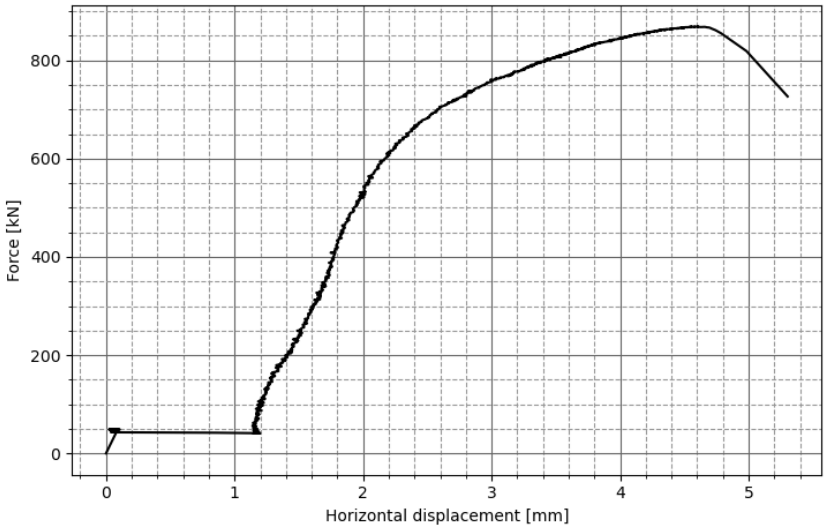

FIGURE 5.5: Force vs. relative in-plane horizontal displacement between the top and the bottom of the chord for specimen C1B10M90.

5.2.4 C1B09M70

To avoid the issue with contact between the dead load and the base plate, the length of the steel rod, which the dead load was attached to, was adjusted. Except for this, nothing about the setup was changed. The dead load attached to the end of the brace in C1B09M70 was about 927 kg, which resulted in an in-plane bending moment of about 4.65 kNm. The ultimate compression load was only slightly smaller than for C1B10M90, reaching about 862 kN, but a different mechanism of failure was observed. As can be seen in Fig. 5.6, the specimen failed due to plastic failure of the chord face. Since the expected failure mode for joints with $\beta \geq 0.85$ is chord wall failure, this was not expected, but it could be due to the influence of welding induced residual stresses in the joint.

5.2.5 C2B10M70

The specimen C2B10M70 was tested with a constant in-plane bending moment from the brace of 1.43 kNm and it reached an ultimate compression load of about 539 kN. However, it became apparent that the influence of the bending moment was minimal. As can be seen in Fig. 5.7, the impact was so small that the elastic local buckling, which led to failure of the specimen, happened outside the region of the joint. However, this might also indicate that the failure occurred due to a local imperfection.

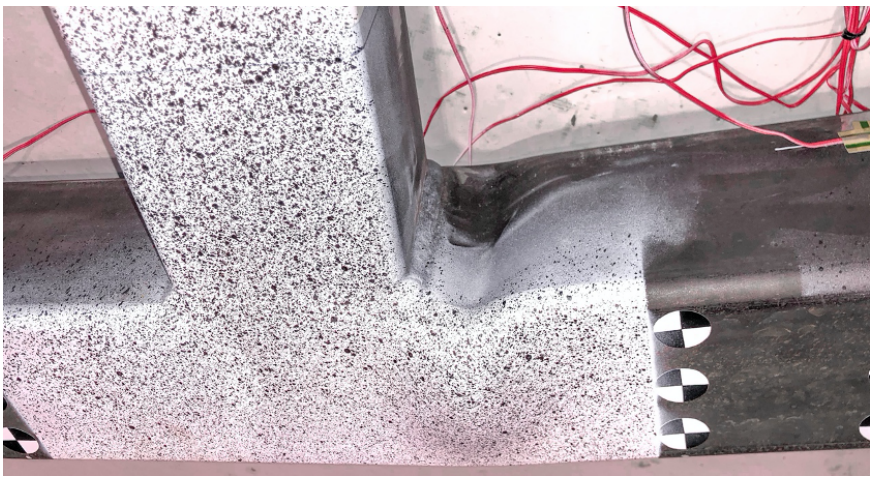

FIGURE 5.6: Plastic failure of the chord face in specimen C1B09M70.

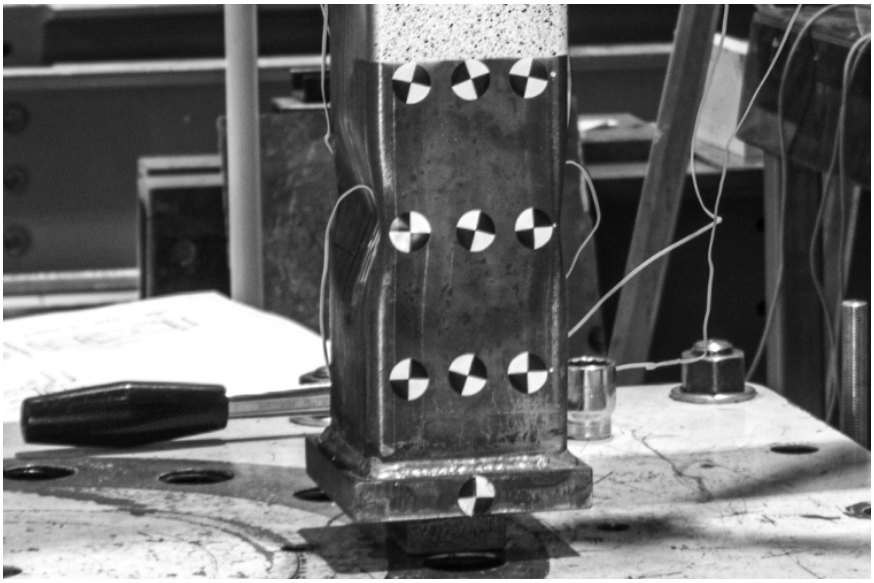

FIGURE 5.7: Failure of specimen C2B10M70 due to elastic local buckling.

5.2.6 C2B10M90

The specimen C2B10M90 was made from the same RHS members as the previously tested specimen C2B10M70, but the in-plane bending moment from the brace was increased to 1.83 kNm. Despite the higher bending moment, a slightly larger ultimate compression load was reached, going to about 544 kN. As can be seen in Fig. 5.8, the elastic local buckling occurred in the chord walls just below the region were the brace was connected. However, since the

ultimate compression load was actually higher than for the previous specimen, where the buckling occurred in a totally different place, it is reasonable to assume that the elastic local buckling stress is close to being reached for the entire chord.

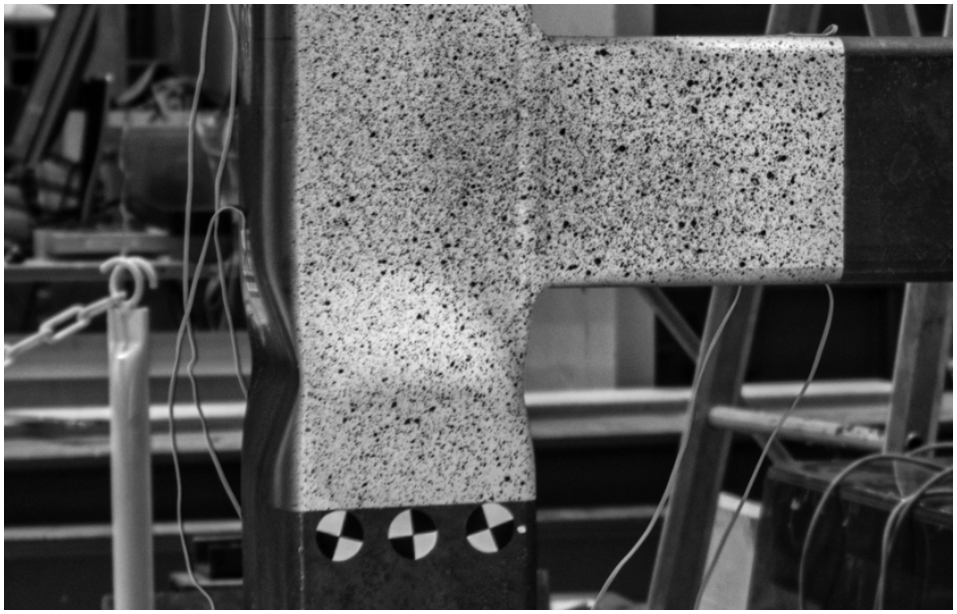

FIGURE 5.8: Failure of specimen C2B10M90 due to elastic local buckling.

5.2.7 C2B09M70

The specimen C2B09M70 was tested with a constant in-plane bending moment from the brace of 2.26 kNm and it reached an ultimate compression load of about 535 kN. Compared to the C2B10-specimens, C2B09M70 had a larger bending moment and lesser rotational stiffness due to the lower β-value. As a result of this, the vertical movement of the end of the brace at the point of failure is almost twice as big, measured as 4.60 mm[1]. In spite of this, the ultimate compression load which was reached is only slightly smaller, which indicates that the influence of the bending moment was still very low. Similarly as for the specimen C2B10M90, the elastic local buckling occurred in the chord walls just below the region were the brace was connected.

[1]Measured relative to the vertical movement in the bottom of the chord

5.2.8 C2B09M90

The specimen C2B09M90 was made from the same RHS members as the previously tested specimen C2B09M70, but the in-plane bending moment from the brace was increased to 2.91 kNm. Similarly as for the other C2-specimens, the increase of the bending moment had a minimal impact on the ultimate compression load, which reached about 531 kN. Just like for the specimens C2B10M90 and C2B09M70, the elastic local buckling occurred in the chord walls just below the region were the brace was connected.

5.2.9 Summary of the test results

A summary of the test results, showing the maximum load and the vertical displacements at the top of the column and the end of the beam at the point of failure, are listed in Table 5.1. Since sideways and vertical displacement at the bottom connection was not fully restricted, relative measurements was used. The vertical displacements was measured relative to the vertical displacement in the bottom of the chord, the horizontal displacement of the top of the chord was measured relative to the horizontal displacement in the bottom of the chord and the horizontal displacement of the end of the brace was measured relative to the average horizontal displacement of the top and the bottom of the chord.

TABLE 5.1: Summary of the test results.

	F_{beam} [kN]	M_{Ed} [kNm]	$N_{\text{u,chord}}$ [kN]	$\delta_{\text{u,chord}}$ [mm]	$\delta_{\text{u,brace}}$ [mm]
C1B10M70	5.98	3.06	626.6	2.91	3.35
C1B10M90	9.31	4.76	868.7	3.46	9.27
C1B09M70	9.10	4.65	861.5	3.40	7.54
C1B09M90	8.61	4.40	608.1	4.54	9.51
C2B10M70	2.79	1.43	539.3	2.41	2.32
C2B10M90	3.59	1.83	543.5	2.23	2.47
C2B09M70	4.42	2.26	534.5	2.27	4.60
C2B09M90	5.69	2.91	531.4	2.28	5.30

The horizontal and vertical displacement of the top of the chord and the end of the brace, with the measured relative to the movement of the specimen as described earlier, are illustrated in Figs. 5.9 and 5.10. Since the first specimen that was tested, C1B10M70, was repositioned after the sudden unloading at 102 kN, the recorded displacements was set to zero when the test was restarted.

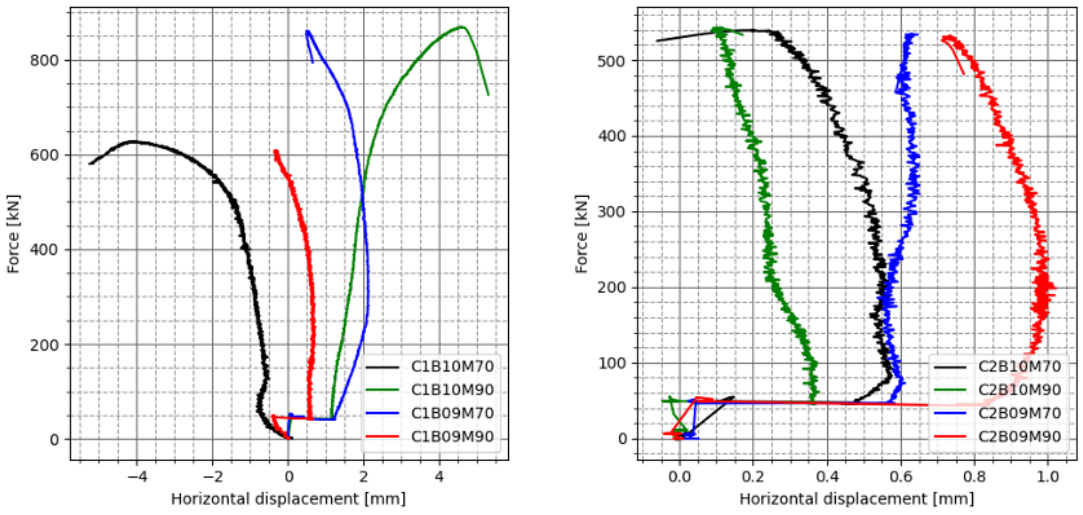

(a)

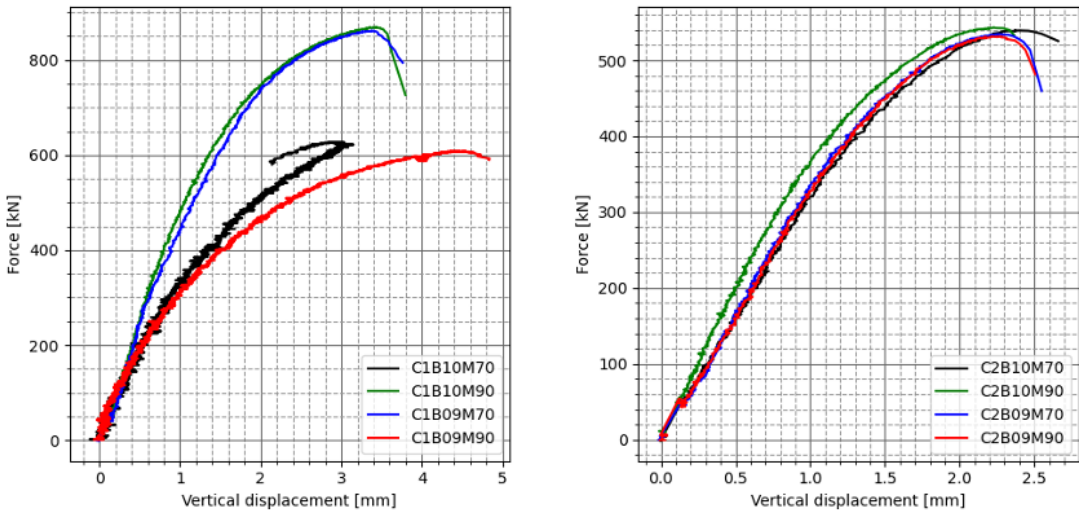

(b)

FIGURE 5.9: Force vs. (a) relative horizontal and (b) relative vertical displacement between the top and the bottom of the chord.

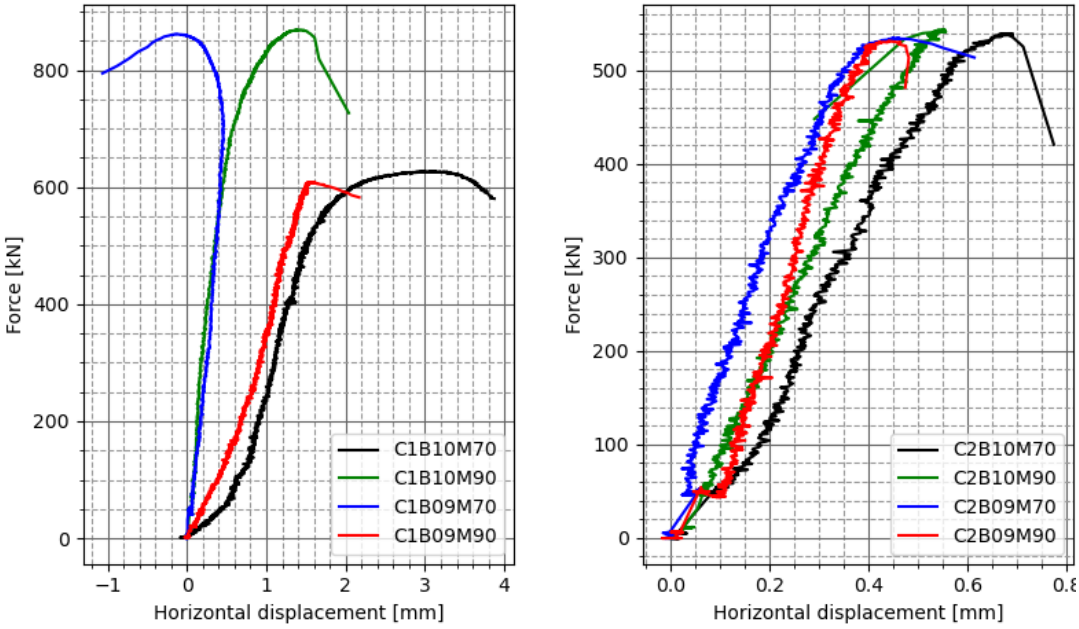

(a)

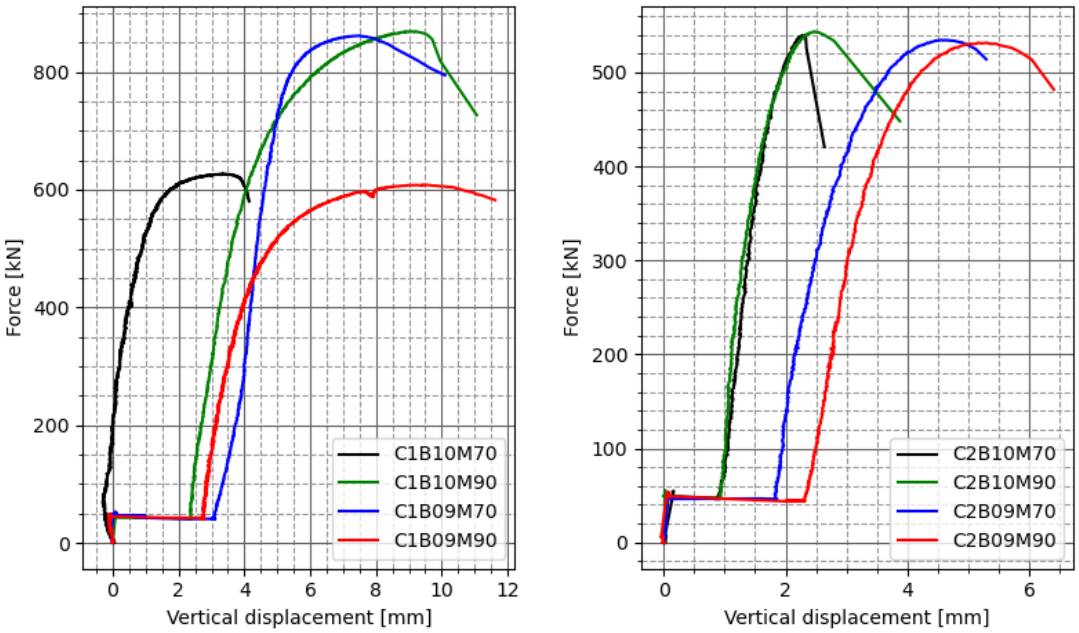

(b)

FIGURE 5.10: Force vs. (a) relative horizontal and (b) relative vertical displacement of the end of the brace.

The specimens with chords in class 4 were expected to fail due to elastic local buckling in the joint region in which the loads from the brace were transferred to. However, the tests revealed that the influence of the bending moment from the brace was minimal, with all of the specimens failing at nearly the same compression load. This was particularly obvious by looking at the failure of specimen C2B10M70, shown in Fig. 5.7, where the buckling which led to failure of the specimen, occurred far away from the region in which the brace was connected to the chord.

In contrast to the C2-specimens, the specimens with chords in class 1, can fully develop the plastic capacity of the section. The expected mechanism of failure for these specimens was chord wall failure, but the specimen C1B09M70 failed due to plastic failure of the chord face, possibly due to the influence of welding induced residual stresses. In addition, the specimen C1B10M70 failed prematurely close to the boundary condition as a consequence of the extra moment introduced due to the lack of lateral stability.

5.3 Comparison and discussion

Based on the results from the tests, it is apparent that the joint design formulas are very conservative for predicting the allowed compression force in the chord when the in-plane bending moment from the brace is close to the allowed design moment resistance. As can be seen in Table 3.7, there is a significant drop in the predicted compression resistance when increasing the moment utilization from 70 to 90 %. The reason for this, is found by looking at the chord stress function, Q_f. Since an exponential decay formula are used in this function, the allowed compression force in the chord drops rapidly as the moment utilization of the joint goes towards full utilization.

In Fig. 5.11, the formula for the joint moment resistance is plotted as a function of the moment utilization and the chord stress ratio, together with the results from the tests. In contrast to the design formulas, the in-plane bending moment from the brace did not have a large influence on the maximum compression force in the chord for any of the specimens which were tested. This deviation might be a consequence of the research which the chord stress function is based on. As described in Chapter 2, the chord stress function is based on test results on joints with a β-value of 0.6, which might not be accurate for large β-values because of the difference in the failure mechanism. The new test results might therefore indicate that the loads from the brace

are transferred to the chord in a more efficient manner and thus making it possible to allow for higher loads in the brace.

TABLE 5.2: Comparison between the design resistance and the experimental results at the ultimate load capacity.

	$N_{u,exp}$ [kN]	$N_{M,Rd}$ [kN]	$\frac{N_{u,exp}}{N_{M,Rd}}$
C1B10M70	626.6	589.3	1.06
C1B10M90	868.7	475.3	1.83
C1B09M70	861.5	658.2	1.31
C1B09M90	608.1	227.0	2.68
C2B10M70	539.3	492.4	1.10
C2B10M90	543.5	301.3	1.80
C2B09M70	534.5	409.9	1.30
C2B09M90	531.4	155.6	3.42

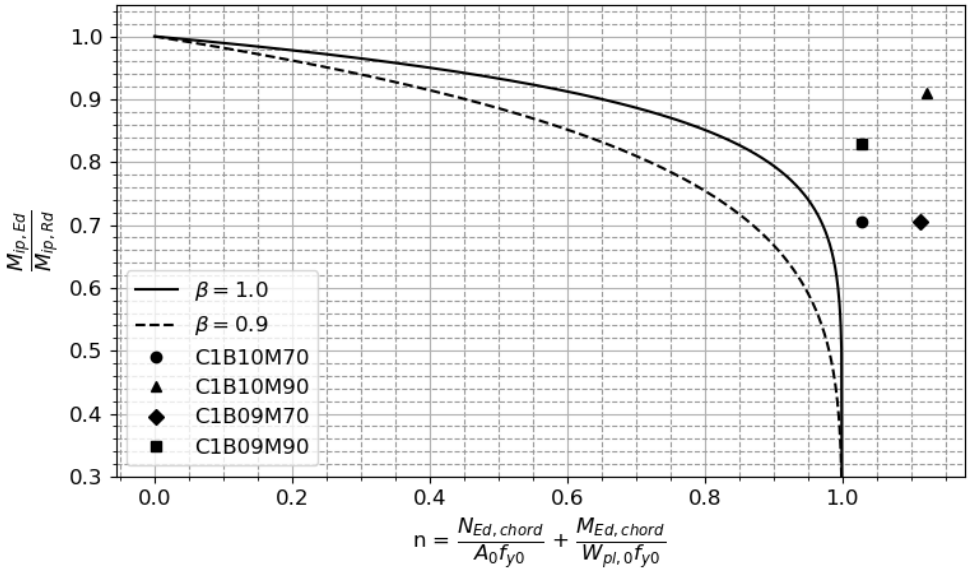

(a)

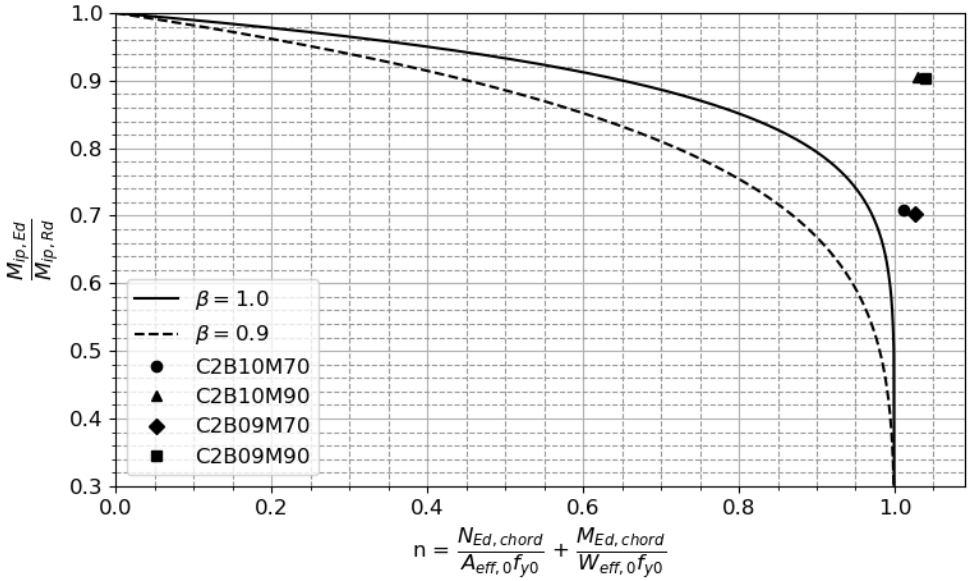

(b)

FIGURE 5.11: Comparison between the design formula and the test results.

Chapter 6

Numerical study

6.1 Introduction

With the use of a finite element analysis (FEA), the behavior of the RHS joints can be simulated and analyzed. Compared to the experimental approach, which can be both time consuming and expensive, FEA makes it possible to effectively test a large number of numerical parameters. However, when doing an FEA, it is often necessary to make some idealizations or assumptions of the material model and the boundary conditions. Another issue particularly relevant for nonlinear FEA is that the solution space is very large, and it is important to ensure that the simulation captures the right deformation mode. Therefore, to ensure that the finite element model accurately predict the experimental behavior, it should be calibrated and validated with experimental test results.

In this chapter, a finite element model for predicting the behavior of RHS T-joints of similar width, with an axial compressive load in the chord and an in-plane bending moment from the brace, is developed. The model was calibrated and validated with the experimental results presented in Chapter 5.

6.2 Construction of the finite element model

The finite element models were created in the non-linear finite element analysis software Abaqus, with the use of continuum shell elements and geometric and material nonlinearities incorporated in the model.

6.2.1 Material properties

The nonlinear material properties were defined with von Mises yield criterion and isotropic hardening, based on the true stress-strain curves obtained from the tensile tests, and the elastic material properties were defined with Young's modulus, $E = 210\,000$ MPa and Poisson's ratio, $v = 0.3$.

As described in Chapter 4, the cold forming results in different material properties around the rectangular hollow section. To account for this, different plastic material properties were assigned for the different faces and the corner regions corresponding to the results found in the material test. Because the corner regions were not tested, it was assumed that these regions had 22 % higher yield stress and 16 % higher tensile strength than the average flat faces, as suggested by Hancock et al. (2005).

6.2.2 Model geometry and idealizations

In general, the overall dimensions of the models were in correspondence to the actual dimensions of the specimens in the experimental program, but some idealizations were implemented to simplify the modelling process and reduce the computational effort. One of these idealizations was on the steel plates which were welded to the top and bottom of the chord and at the end of the beam, since these plates are difficult to model with shell elements. The behavior of these regions was therefore approximated by creating a reference point in the midpoint of the sections in the correct distance from the end of the hollow sections, as shown in Fig. 6.1. With the use of a coupling constraint, the kinematic degrees of freedom at the RHS surface could then be coupled to the reference point.

Furthermore, the weld geometry at the intersection between the brace and the chord can be very complicated and difficult to model accurately and it was therefore decided to use a tie constraint to model the weld. According to Lee (1999), the use of weld-effect models generally make little difference to the overall behavior and strength of RHS T-joints and is therefore not a necessary feature of such joint models. However, shell models excluding the weld geometry cannot be used to accurately reproduce the near field stresses, but they can be used to reproduce the far field stresses in an accurate manner.

The tie constraint was created by defining two surfaces, a master surface in the weld leg of the brace and a slave surface in the weld leg of the chord. To simulate the butt weld, the edge of the brace was defined as the master

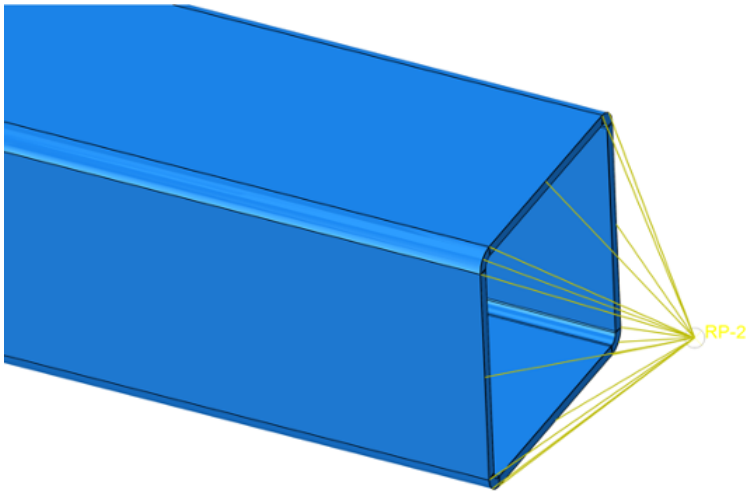

FIGURE 6.1: Reference point with coupling constraint to the end of the shell RHS (thickness visually rendered).

surface, while for the fillet weld the master surface was defined in the walls of the brace as shown in Fig. 6.2. The master and slave surfaces were tied together with a specified position tolerance, such that there was no relative motion between them. This also makes it possible to use independent meshes for the two connected members, which further simplifies the modelling process.

6.2.3 Finite element mesh

Each of the specimens was modelled with S4R elements, which are a four-node, quadrilateral stress/displacement shell element with reduced integration, and the Simpson thickness integration rule with five integration points through the thickness. For strength analysis, shell elements might be preferable to solid elements due to being computationally less expensive. According to the Abaqus documentation (2014), the CPU time for a linear implicit analysis is approximately proportional to the square of the number of degrees of freedom. When modelling with solid elements, a minimum of 3 to 4 elements across the thickness is necessary to obtain an accurate solution, while for shell elements the wall thickness is not actually modelled but captured as a mathematical value, such that the required number of elements are much lower (Broekaart, 2016). Consequently, the use of shell elements makes it possible to create a cheaper but accurate simulation.

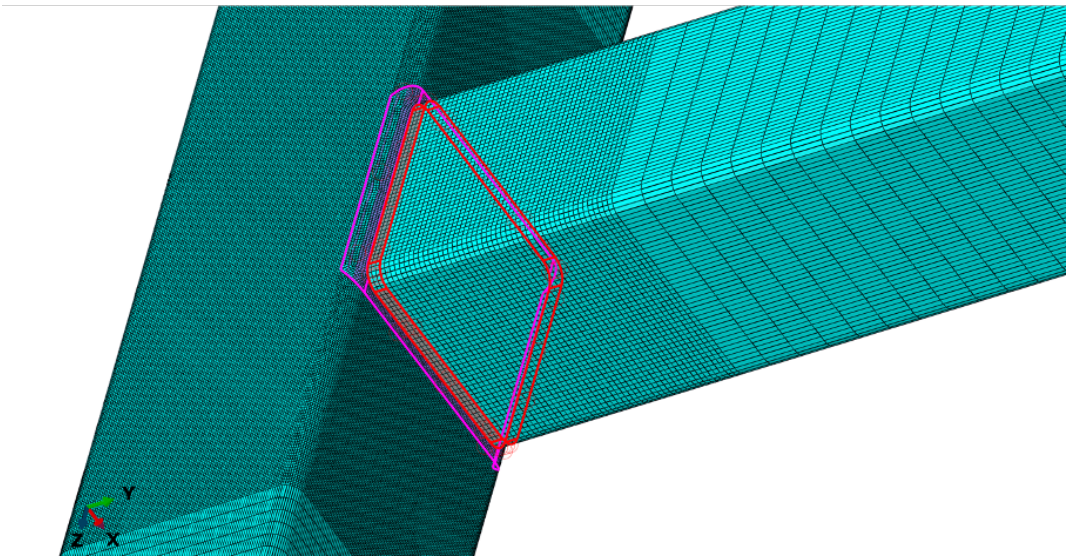

FIGURE 6.2: Tie constraint between the chord and the brace for a joint with β-value 0.9, with the slave surface in purple and the master surface in red.

The choice of finite element size was focused on finding a good balance between getting accurate results and keeping the computational demand low. Several analyses were therefore performed to evaluate the increase in accuracy versus the increase in computational time for different element sizes. An effective way to increase the accuracy, without significantly increasing the computing time, is to refine the mesh only in regions were high deformations or high stresses occur. Since the maximum stresses are found in the region near the joint, the mesh in this region was refined as illustrated in Fig. 6.3. The recommended mesh size was determined to be 2 mm in the refined region and 4 mm elsewhere. A structured mesh was used for the entire model, except for the region on the chord in which the tie constraint was defined. Since this region was partitioned to define a suitable region for the tie constraint, the topology of this region was too complex for a structured mesh. To resolve this, a free meshing was utilized.

6.2.4 Boundary conditions and simulation for the loading

The boundary conditions in the finite element model deviate somewhat from the specimens in the experimental work, since it was decided not to model the steel plates connecting the RHS members to the test frame. Instead, a pinned connection was created in the top and bottom of the chord by constraining the degrees of freedom at the previously described reference points.

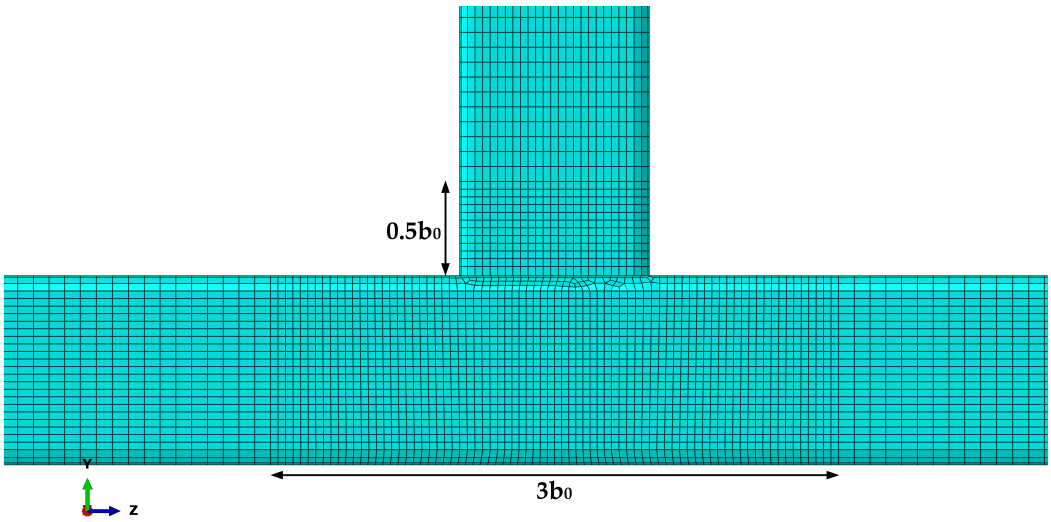

FIGURE 6.3: Regions with refined mesh size.

As opposed to the specimens in the experimental work, this creates a perfect hinge which can resist both vertical and horizontal forces but is free to rotate.

The loading was simulated by applying concentrated forces at the reference points in the top of the chord and at the end of the brace in the same sequence as in the experimental joint tests. The initial compression load in the chord and the brace load was configured with a static general procedure, while a static Riks procedure was used for the last step of compression in the chord. Riks procedure is generally used to predict unstable, geometrically nonlinear collapse of a structure, which is done by simultaneously solving for loads and displacements (Corp., 2014). Compared to a static general analysis, which can only take incremental steps (positive stiffness matrix), Riks analysis is also able to follow declining paths of negative stiffness.

6.3 Calibration of the finite element model with the experimental results

To minimize the difference between the numerical and the experimental results, the finite element model should be calibrated with the experimental results. When deciding which parameters to investigate, attention was paid on identifying parameters that were not measured with absolute confidence and which might have had an effect on the numerical results. Three different parameters were identified as follow:

- The definition of the tie constraint used to simulate the weld,
- The material properties of the corner region,
- The thickness of the RHS members.

6.3.1 Tie constraint

As described in Section 6.2, the tie constraint was created by defining a master surface in the weld leg of the brace and a slave surface in the weld leg of the chord. However, since the region of the weld legs was not measured exactly and the weld geometry of the weld was quite complicated due to the rounded corners, there was some uncertainty in the size of these regions. For this reason, it was decided to investigate this effect by altering the size of the weld region.

The initial plan was to examine the behavior of the weld by measuring the relative displacement between points just outside the weld in the brace and the chord, as illustrated in Fig. 6.4. The experimental data in this region was meant to be captured by the 3D-DIC, but unfortunately there were some issues with the accuracy of these data, except for specimens C1B10M70 and C1B09M90, which was tested prior to the other specimens. Since C1B10M70 had large lateral displacements, both in-plane and out-of-plane, it was unsuited for doing the calibration, which left only C1B09M90.

However, there is a significant difference between the welding of the RHS members of equal width and the members with $\beta = 0.9$, such that the weld had to be checked for both. To evaluate the specimens with $\beta = 1$, it was therefore decided to include specimen C1B10M90 and use the data from the subsets.

For the specimen C1B09M90, three different configurations were tested and compared against the experimental results. In the first and second configuration, the weld-foot was set equal to 5.6 mm and 4 mm respectively, for both the fillet weld and the partial butt weld. Since the corner radius was 7 mm, this resulted in a weld that was not entirely flush with the chord face. To achieve such a weld, without also increasing the size of the fillet weld, two separate tie constraints were created in the third configuration keeping the fillet weld with a weld-foot of 5.6 mm.

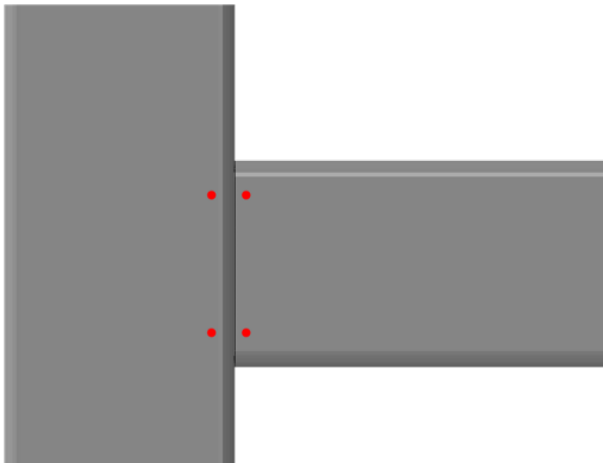

FIGURE 6.4: Points used for evaluating the weld behavior.

As can be seen in Fig. 6.5, the FE models seem to capture the behavior of the weld quite well and in addition, the difference between the various configurations was relatively small, being almost negligible for the vertical displacement. For the horizontal displacement, a small effect was observed in the different configurations, but it is difficult to identify which one is most accurate since in comparison to the experimental results, the horizontal displacement is larger for the upper points and smaller for the bottom points. It might be possible to capture this effect in the FE model by adjusting the weld region such that it is asymmetrical, but since the difference was relatively small this was deemed unnecessary.

For the specimens with $\beta = 1$, a partial butt weld is used to weld the edge of the brace to the chord. However, it is difficult to be certain as to the depth of the penetration without making a cut through the welded connection, which was only done for specimen C1B10M70. To evaluate the influence of the depth of the penetration of the butt weld, three different weld configurations were tested and compared against the experimental results for specimen C1B10M90. The entire corner radius, half the corner radius and a quarter of the corner radius was used as weld-foot, respectively, while the fillet weld was fixed at 5.6 mm for all the configurations. The results are illustrated in Fig. 6.6.

At first glance, it seems that there is a significant deviation between the FE models and the experimental result, especially for the vertical displacement. However, as shown previously in Fig. 5.5, sideways movement at the top and bottom connection is not fully restrained, such that a small rotation is introduced which affects the results. Because the boundary conditions in the FE

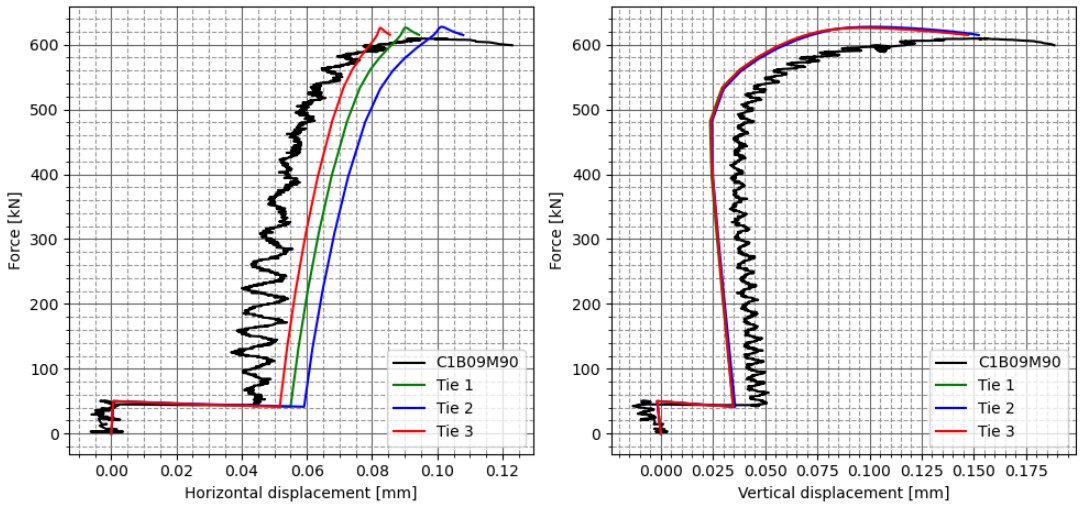

(a) Upper points

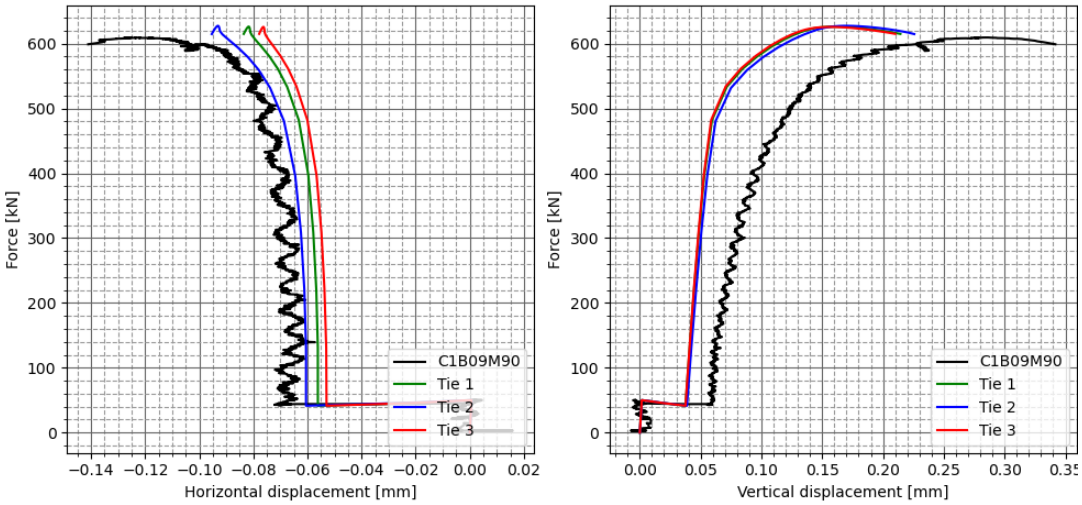

(b) Lower points

FIGURE 6.5: Force vs. relative displacement between points on different sides of the weld showing the effect of different configurations of the tie constraint.

model is constrained against sideways movement, this rotation is not replicated in the model. However, since the sideways movement in the top and bottom of the chord in the experiments was measured, the effect of the rotation can be calculated and subtracted from the experimental results. The angle of the rotation, θ, and the resulting horizontal and vertical displacement of the brace, δ_u and δ_v, can be calculated with the formulas:

$$\theta = \tan^{-1} \frac{\Delta_u}{l_1} \tag{6.1}$$

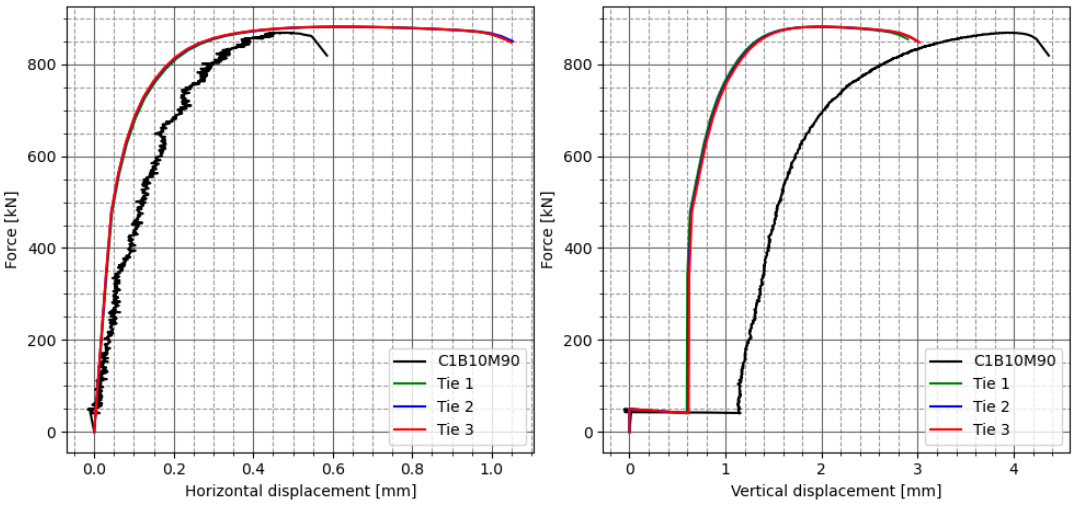

FIGURE 6.6: Force vs. relative displacement between the brace and the chord.

$$\delta_u = l_2 \sin\theta \tan\theta \tag{6.2}$$

$$\delta_v = l_2 \sin\theta \tag{6.3}$$

where:

Δ_u, is the relative displacement between the top and bottom of the chord,

l_1, is the distance between the subsets at the top and bottom connection,

l_2, is the distance between the subsets at the chord and the brace.

As can be seen in Fig. 6.7, a much better fit between the experimental results and the FE models is attained. It can also be seen that the difference between the three different configurations of the weld in the FE models is minimal.

6.3.2 Material properties of the corner region

Since the properties of the material in the corner regions were not tested, it was assumed that these regions had 22 % higher yield stress and 16 % higher tensile strength than the average flat faces as suggested by Hancock et al. (2005). However, the coefficient of variation was reported to be 0.0727 for the

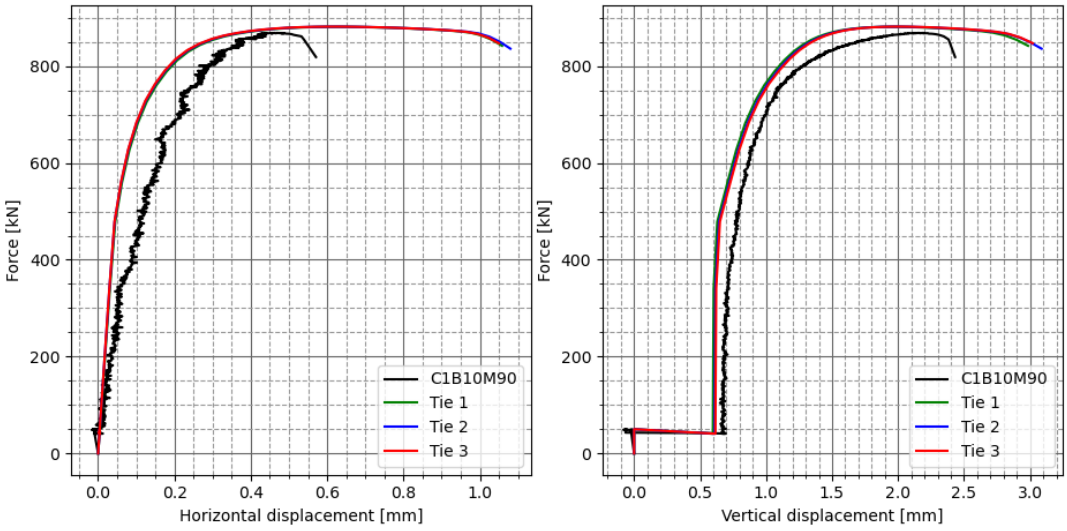

FIGURE 6.7: Force vs. relative displacement between the brace and the chord, corrected for the sideways movement of the top and bottom connection.

yield stress and 0.0575 for the tensile strength, which indicates that the level of dispersion around the mean is quite high.

To examine the influence of the material properties in the corner region, it was decided to test three different configurations within the range of variability reported by Hancock et al. (2005):

1. 22 % higher yield stress and 16 % higher tensile strength,
2. 15 % higher yield stress and 10 % higher tensile strength,
3. 29 % higher yield stress and 22 % higher tensile strength.

The test was performed for the specimens, C1B09M90 and C2B10M90, which had chords in class 1 and 4, respectively. To evaluate the different configurations, the vertical displacement between the top and bottom of the chord and the end of the brace and the middle of the chord was examined. Similarly as in Section 6.3.1, the displacement due to the rotation of the specimens was subtracted from the experimental results.

As can be seen in Fig. 6.8, the adjustment of the material properties of the corner region had a a visible effect on the ultimate load, resulting in a difference between configuration 1 and 3 of about 17 kN for C1B09M70 and about 11 kN for C2B10M90. There is a good fit between the experimental results and the

FE models for C1B09M70, both for the ultimate load and the decrease in stiffness due to the plasticity effects, while for C2B10M90 the ultimate load in the FE models is significantly higher than in the experiment.

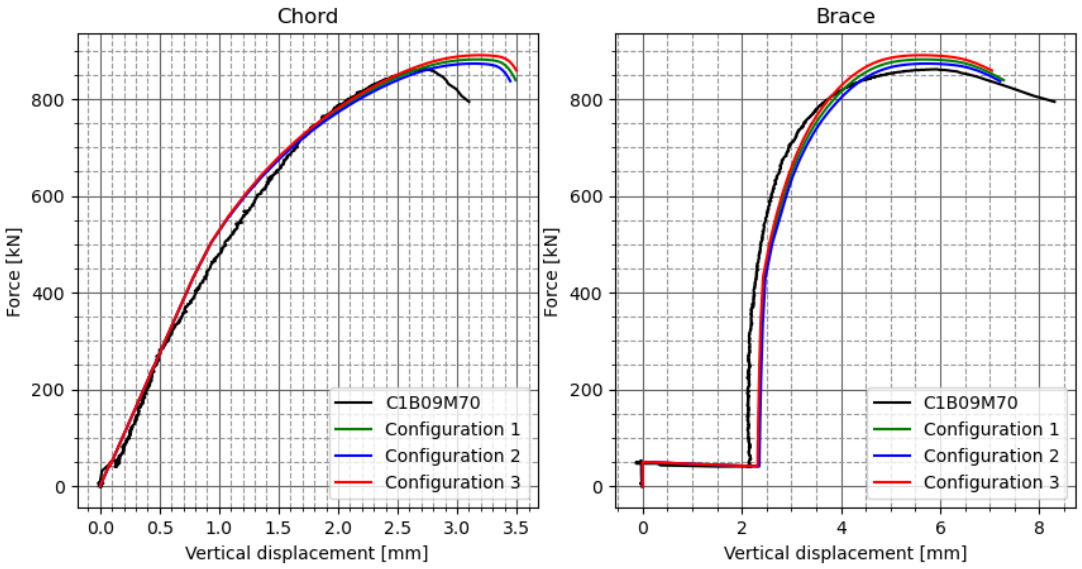

(a) C1B09M70

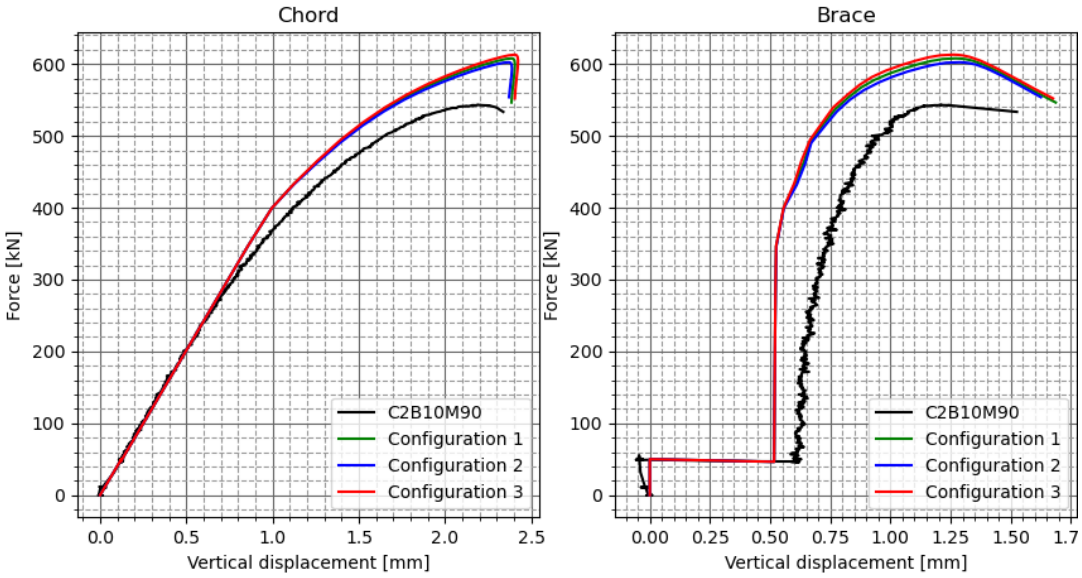

(b) C2B10M90

FIGURE 6.8: Force vs. relative displacement between subsets in the chord and the brace, showing the effect of different configurations of the material properties in the corner region.

6.3.3 Thickness of the RHS members

Since the joints in the experimental work came with steel plates welded to the end of the RHS members, it was impossible to measure the thickness

directly on the specimens. Instead, the thickness was measured from the corresponding RHS spare parts which were used in the material testing. It was first measured with a micrometer and in addition, after the parts had been cut into coupons, the thickness of each of the coupons were measured with a digital caliper. Since the same thickness was measured, it was expected that these two measurements would be similar, but as can be seen in Tables 3.2 and 4.1, there was a significant difference.

The thickness of the RHS members should have a considerable effect on the results and it was therefore decided to examine the impact of a change in thickness. Three different configurations, as listed in Table 6.1, were tested for the specimens C1B09M90 and C2B10M90.

TABLE 6.1: Thickness of the chord and the brace for the different configurations.

	C1B09M70		C2B10M90	
	t_{chord} [mm]	t_{brace} [mm]	t_{chord} [mm]	t_{brace} [mm]
Config. 1	4.08	3.84	2.96	4.08
Config. 2	4.00	3.76	2.89	4.00
Config. 3	3.93	3.69	2.82	3.93

As can be seen in Fig. 6.8, there was a significant difference between the different configurations. Especially for the specimen C2B10M90, a much better fit with the experimental results was achieved with configuration 3, which had the lowest thickness. Since the ultimate load is considerably overestimated for configuration 3, where the thickness corresponded to the measurements performed with the micrometer, it might be reasonable to assume that the thickness measured from the coupons was more correct. The reason for this is uncertain, but could be related to measurement errors, for example due to misreading of the micrometer or inaccurate setting of the zero reading.

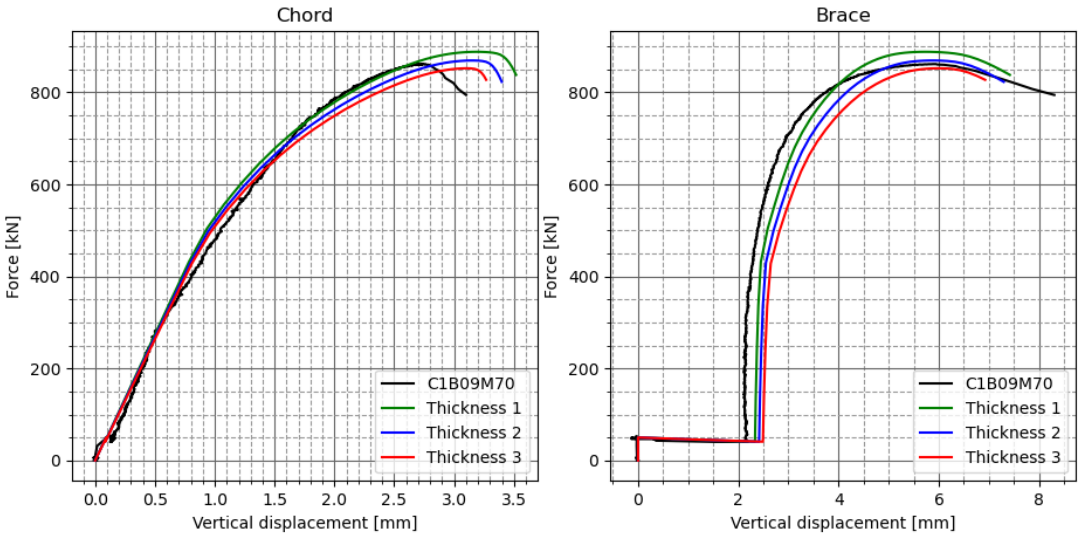

(a) C1B09M70

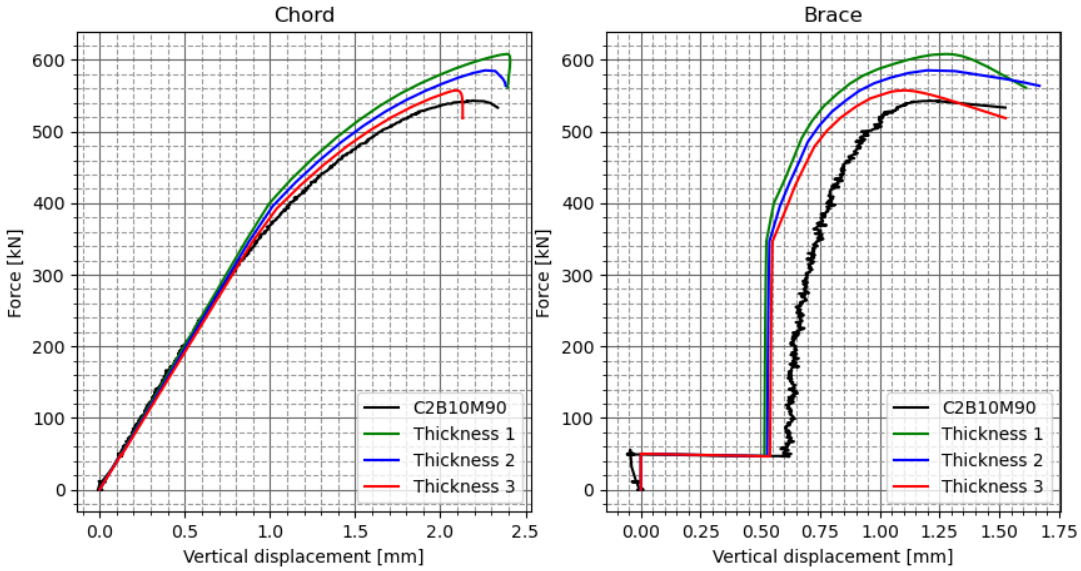

(b) C2B10M90

FIGURE 6.9: Force vs. relative displacement between subsets in the chord and the brace, showing the effect of different configurations of the thickness.

6.3.4 Summary and conclusion

In this section, different configurations of the tie constraint, the material properties of the corner region and the thickness of the RHS members was evaluated against the experimental results. It was found that the different configurations of the tie constraint had a relatively small effect, but that the behavior of the weld was well predicted by the FE models. It was decided to model the tie constraint with a leg size of 5.6 mm for the fillet weld, while for the partial

butt weld, the weld-foot matched the entire corner radius for the specimens with $\beta = 0.9$ and half the corner radius for the specimens with $\beta = 1.0$.

The material properties of the corner was found to have some influence on the ultimate load, but did not have a significant effect on the vertical deformations. Based on the results, it was decided to use the average value with 22 % higher yield stress and 16 % higher tensile strength than the average of the flat faces for all of the RHS members, except for the B×100×3 profile. Compared to the other profiles, B×100×3 was about 1 mm thinner, but the corner radius was measured to be nearly equal. This might indicate that the corners of this profile were subjected to less strain-hardening in the cold forming process, which leads to a lesser increase in yield stress and tensile strength compared to the other profiles. In addition, it was shown in Fig. 6.9b that the ultimate load was larger for all the three configurations. Consequently, it was decided to model the RHS profile, B×100×3, with 15 % higher yield stress and 10 % higher tensile strength than the average of the flat faces.

When evaluating different configuration of the thickness of the RHS members, it was found that the experimental results were most accurately reproduced with the thickness measured from the coupons, as listed in Table 4.1. For this reason, it was decided to use these values in the FE model.

6.4 Validation of the finite element model with the experimental results

To make sure the developed FE model could be used to predict the structural behavior of RHS T-joints, it should be validated with experimental tests. With the model constructed according to the above findings, the validation was performed by comparing the vertical force-displacement curves of the chord and the brace of the FE model with the experimental results on the joints[1].

The axial deformation of the chord was measured as the displacement of the top of the chord relative to the bottom of the chord, while the deformation of the brace was measured as the differential vertical displacement of the end of the brace relative to the middle of the chord in which the brace was connected.

[1]Since the specimen C1B10M70 had large displacements both in-plane and out-of-plane, it was excluded from the validation.

As described in Section 6.3, minimal lateral displacements of the hinged boundary-conditions induced some rigid-body translation and rotation of the entire specimen. The effect of this rotation was subtracted from the experimental results. The comparison between the numerical and experimental results is shown in Figs. 6.10 to 6.16. In addition, a comparison between the numerical and experimental results with regard to the ultimate load capacity, is listed in Table 6.2.

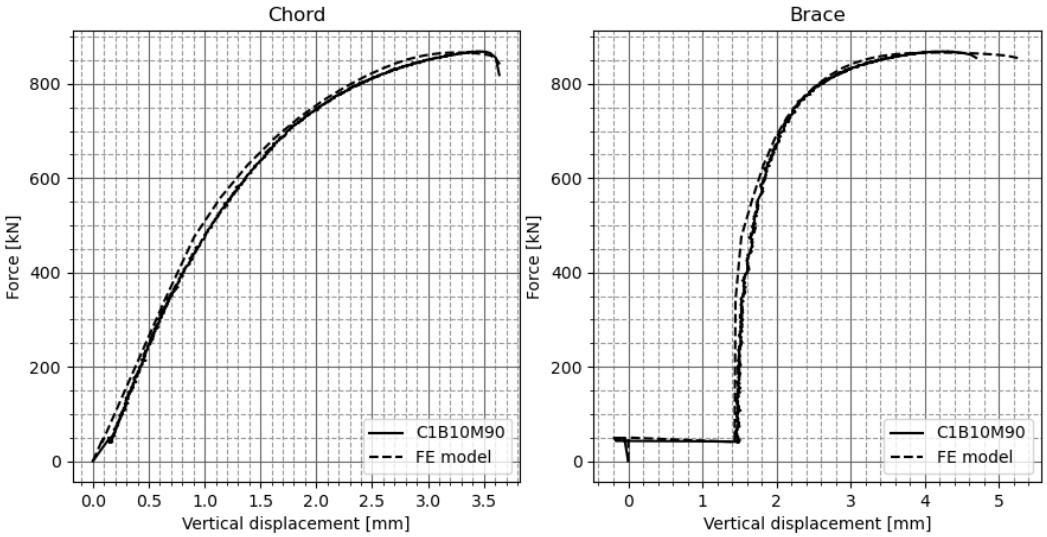

FIGURE 6.10: C1B10M90: Validation of the numerical model with the experimental results.

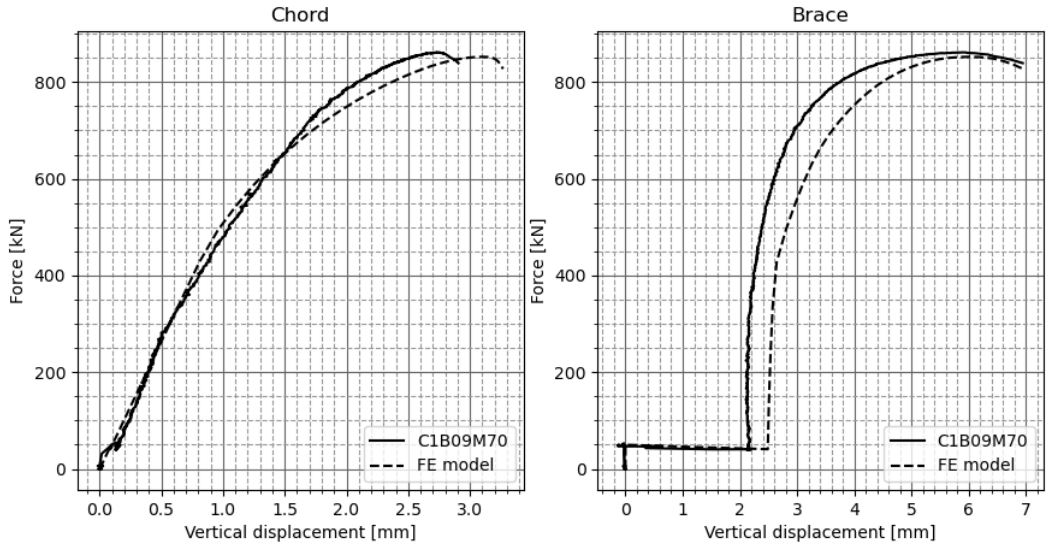

FIGURE 6.11: C1B09M70: Validation of the numerical model with the experimental results.

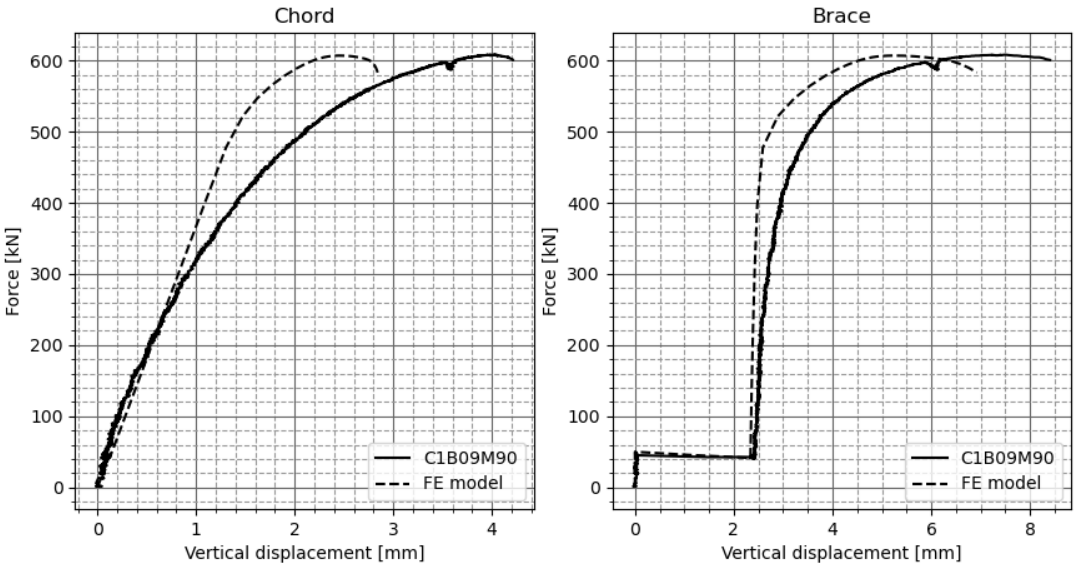

FIGURE 6.12: C1B09M90: Validation of the numerical model with the experimental results.

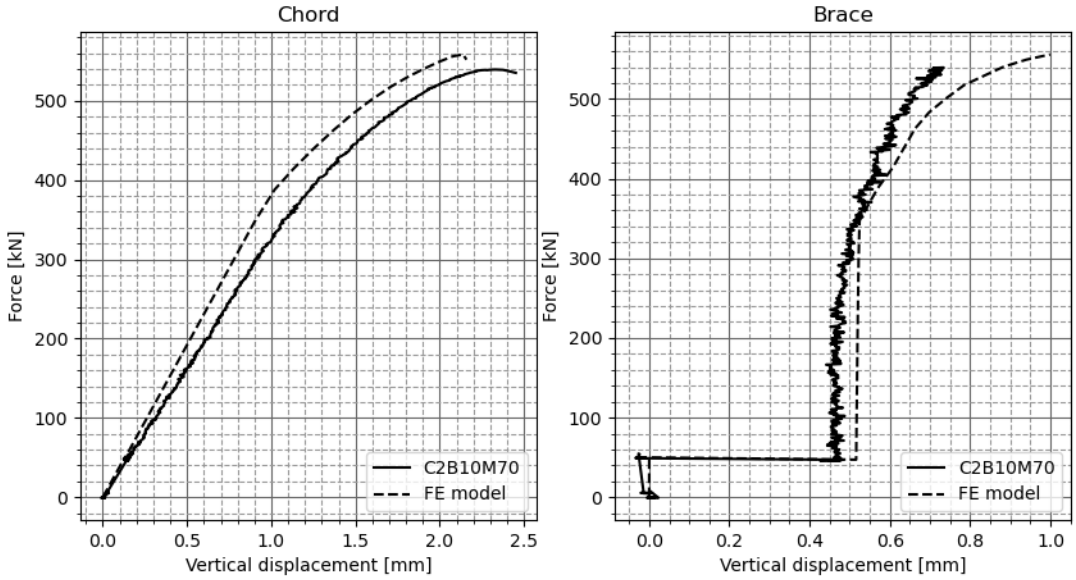

FIGURE 6.13: C2B10M70: Validation of the numerical model with the experimental results.

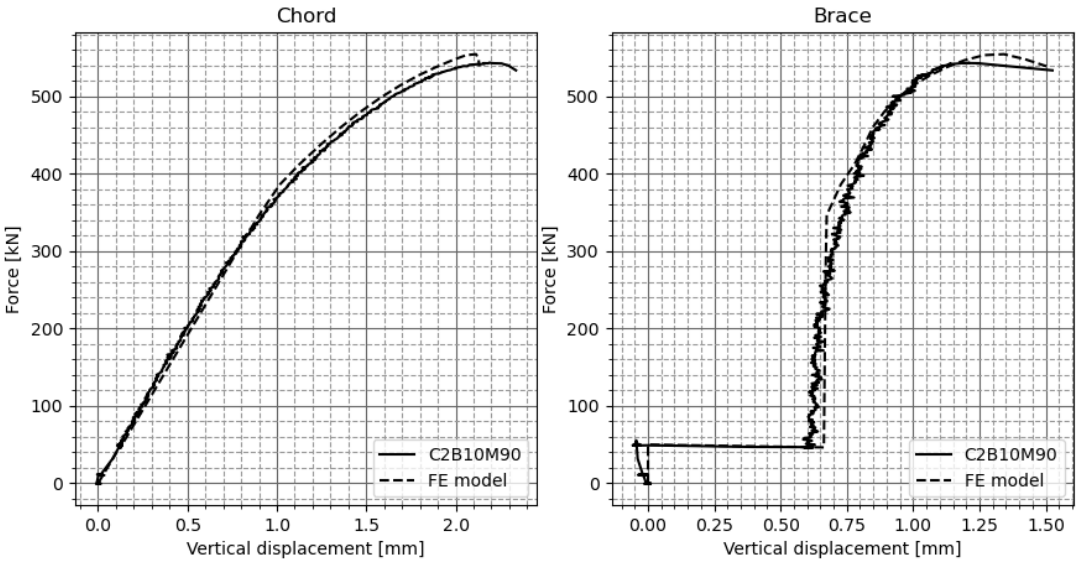

FIGURE 6.14: C2B10M90: Validation of the numerical model with the experimental results.

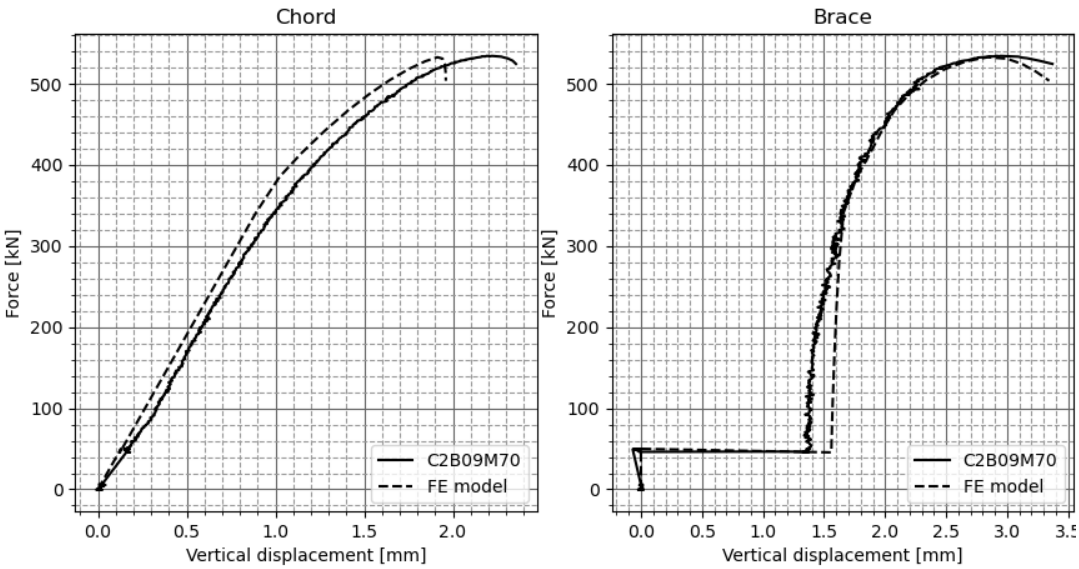

FIGURE 6.15: C2B09M70: Validation of the numerical model with the experimental results.

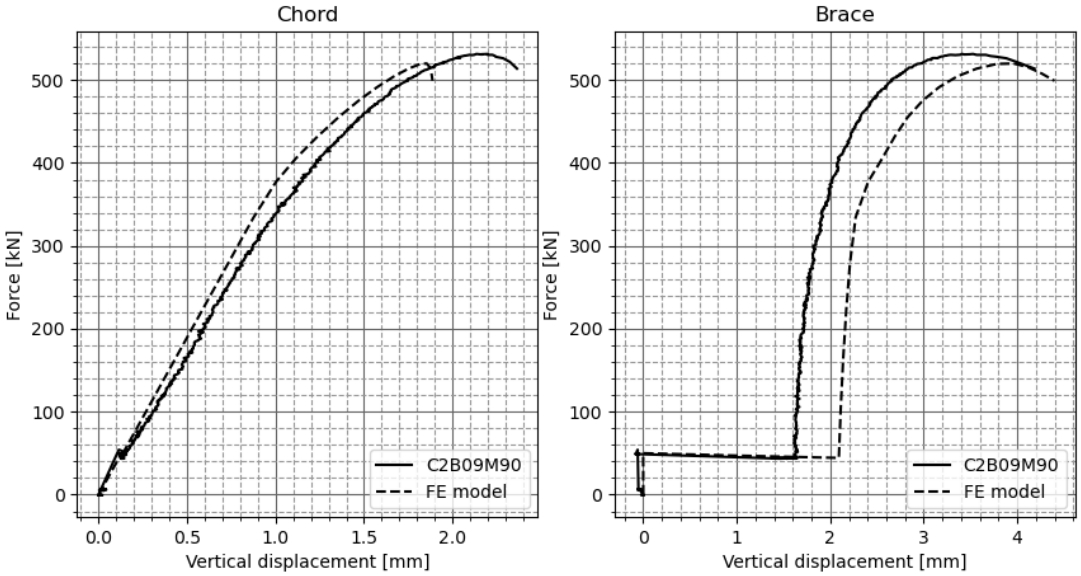

FIGURE 6.16: C2B09M90: Validation of the numerical model with the experimental results.

TABLE 6.2: Comparison between the numerical and experimental results at the ultimate load capacity.

	$N_{u,num}$ [kN]	$N_{u,exp}$ [kN]	$\frac{N_{u,num}}{N_{u,exp}}$
C1B10M90	866.3	868.7	1.00
C1B09M70	852.3	861.5	0.99
C1B09M90	606.9	608.1	1.00
C2B10M70	558.3	539.3	1.04
C2B10M90	554.3	543.5	1.02
C2B09M70	532.8	534.5	1.00
C2B09M90	520.0	531.4	0.98

A good agreement between the numerical simulations and the experimental results is found for most of the cases. The largest deviation between the numerical and experimental results with regard to the ultimate load capacity,

was for the specimen C2B10M70, where the FE model overestimated the load by 4 %. However, it should be noted that despite having the same configuration and a lower in-plane bending from the brace compared to C2B10M90, the ultimate load was found to be slightly lower for C2B10M70 in the experimental tests. In addition, the failure happened outside of the joint region, which might indicate that it failed due to a local imperfection.

With regard to the deformation pattern, the largest deviation is found for C1B09M90. As can be seen in Fig. 6.12,the initial stiffness seem to be correct, but as the load passes 300 kN, the decreasing stiffness is not accurately captured by the FE model. However, as described in Chapter 4, the coupons used in the material test from the profile A-100×4, were cut from the specimen, C1B10M70, after it had been tested. The increased stiffness of the FE model could therefore be due to strain hardening through plastic deformation during the testing of C1B10M70.

Chapter 7

Summary, conclusions and suggestions for further work

7.1 Summary

In this study, the behavior of welded T-joints consisting of RHS members of similar width, with an axial compressive load in the chord and an in plane bending moment from the brace, has been investigated.

Based on the available literature on RHS T-joints, there seems to be no experimental tests performed on RHS T-joints of similar width subjected to a combined loading situation with a compression force in the chord and an in-plane bending moment from the brace. Furthermore, it was found that the chord stress function, Q_f, which is used to account for the reduced moment resistance in the joint due to the presence of axial forces in the chord, is based on experimental results on joints with $\beta = 0.6$. The mode change of the expected failure from chord face failure to chord side wall failure when the β exceeds 0.85, might indicate that this function could be less accurate for joints with β-values between 0.85 and 1.0.

To properly investigate the behavior of RHS T-joints under the conditions described above, experimental tests of four joints with $\beta = 0.9$ and four joints with $\beta = 1.0$ were performed in the laboratory of the Department of Structural Engineering at NTNU. In addition, material test were performed for each of the profiles used to construct the joints, so the design resistance could be calculated with the actual material values and such that the actual

material properties of the RHS members could be incorporated in numerical simulations.

The results from the experimental testing were compared against the design recommendations in prEN 1993-1-8 and it was found that the joint design formulas are very conservative in predicting the allowed compression force in the chord when the in-plane bending moment from the brace is close to the design moment resistance of the joint. In contrast, the in-plane bending moment from the brace did not have a significant influence on the maximum compression force in the chord for any of the joints in the experimental testing. This deviation might be a consequence of the chord stress function being based on test results from joints with a $\beta = 0.6$, which have a different failure mechanism. The new test results might therefore indicate that the loads from the brace are transferred to the chord in a more efficient manner, thus allowing for higher loads in the brace.

Some studies using numerical models to examine the behavior of welded RHS T-joints of similar width submitted to a combined loading situation, already exists. However, due to the previous lack of experimental tests, these models were calibrated with the use of tests on either joints with small β-values, on joints with different load combinations or with the use of analytical formulas. Now that experimental tests on RHS T-joints have been successfully performed, it should be possible to construct FE models which can be properly calibrated and validated. This allows for further investigations, including extensive parametric studies, into the behavior of RHS T-joints.

As a part of this study, a finite element model for predicting the behavior of RHS T-joints of similar width, submitted to an axial compressive load in the chord and an in-plane bending moment from the brace, was proposed. The FE model was created using the non-linear finite element analysis software Abaqus, with the use of continuum shell elements and geometric and material non-linearities incorporated in the model. The constructed FE model was calibrated and validated with the new experimental test results and it was shown that the model was able to predict both the deformation pattern and the resistance of the joints, which justifies the applicability of this model for further investigations.

7.2 Conclusions

The conclusions from this study can be summarized as follow:

- The joint design formulas in prEN 1993-1-8 are very conservative in predicting the allowed compression force in the chord when the in-plane bending moment from the brace is close to the design moment resistance of the joint.
- The in-plane bending moment from the brace did not have a significant influence on the maximum compression force in the chord for any of the joints in the experimental testing.
- An FE model with shell elements can be used to efficiently predict the behavior of RHS T-joints submitted to an axial compressive load in the chord and an in-plane bending moment from the brace.

7.3 Suggestions for further work

Based on this study, some suggestions for further work is presented as follow:

- To better utilize the loading capacity of RHS T-joints, the influence of the in-plane bending moment from the brace on the maximum compression force in the chord should be studied closer.
- The design recommendations for RHS T-joints should be evaluated against the new experimental results.
- Extensive numerical parametric studies should be carried out to examine a broader range of values.

Bibliography

Broekaart, D. (2016). *5 reasons to use a mid-surface shell mesh for thin-walled parts*. URL: https://info.simuleon.com/blog/5-reasons-why-your-fea-simulations-should-be-setup-with-a-mid-surface-shell-mesh-for-thin-walled-parts (Retrieved: 12/06/2020).

CEN/TC 250/SC 3 (2018). *Final document of prEN 1993-1-8*.

Corp., Dassault Systèmes Simulia (2014). *Getting started with Abaqus: Interactive edition*. Providence, RI, USA.

European Commission (2005). *Design rules for cold-formed structural hollow sections*. Office for Official Publications of the European Communities.

Gambhir, M. L. (2013). *Fundamentals of Structural Steel Design*. McGraw Hill Education (India) Private Limited.

Hancock, G., Wilkinson, T. J. and Zhao, X. -L. (2005). *Cold-formed Tubular Members and Connections: Structural Behaviour and Design*. Elsevier Science.

IIW (2009). *Static design procedure for welded hollow section joints – Recommendations*. 3rd ed. Intern. Institute of Welding, Sub-commission XV-E, Annual Assembly, Singapore, IIW Doc. XV-1329-09.

International Digital Image Correlation Society, iDICs (2018). *A Good Practices Guide for Digital Image Correlation*. DOI: 10.32720/idics/gpg.ed1.

Lee, M. M. K. (1999). "Strength, stress and fracture analyses of offshore tubular joints using finite elements". In: *Journal of Constructional Steel Research*, pp. 265–286.

Li, S.H., G. Zeng, Y.F. Ma, Y.J. Guo, and X.M. Lai (2009). "Residual stresses in roll-formed square hollow sections". In: *Thin-Walled Structures 47*, pp. 505–513.

Packer, J. A. (1993). "Moment Connections between Rectangular Hollow Sections". In: *Journal of Constructional Steel Research* 25, pp. 63–81.

Standard Norge (2009). *Eurocode 3: Design of steel structures - Part 1-8: Design of joints*. NS-EN 1993-1-8:2005+NA:2009. Oslo: Standard Norge.

Standard Norge (2015). *Eurocode 3: Design of steel structures - Part 1-1: General rules and rules for buildings*. NS-EN 1993-1-1:2005+A1:2014+NA:2015. Oslo: Standard Norge.

Standard Norge (2019). *Eurocode 3: Design of steel structures - Part 1-5: Plated structural elements*. NS-EN 1993-1-5:2006+AC+A1:2017+A2:2019+NA:2019. Oslo: Standard Norge.

Wang, J.J, N. Gowripalan, J. Li, and V.V. Nguyen (2017). "Close-range photogrammetry for accurate deformation distribution measurement". In: *Mechanics of Structures and Materials: Advancements and challenges* 1, pp. 793–802.

Wang, Y., J. Jiang, C. Wanintrudal, C. Du, D. Zhou, L. Smith, and L. Yang (2010). "Whole field sheet-metal tensile test using digital image correlation". In: *Experimental Techniques* 34, pp. 54–59. DOI: 10.1111/j.1747-1567.2009.00483.x.

Wardenier, J. (1982). *Hollow section joints*. Delft: Delft University Press.

Wardenier, J., J. A. Packer, X. L. Zhao, and G. J. van der Vegte (2010a). "Background of the new RHS joint strength equations in the IIW (2009) recommendations". In: *Proceedings of the 13th International symposium on Tubular Structures*, pp. 402–412.

Wardenier, J., J. A. Packer, X. L. Zhao, and G. J. van der Vegte (2010b). *Hollow Sections in Structural Applications*. Geneve: CIDECT.

Wardenier, J., J. A. Packer, X. L. Zhao, G. J. van der Vegte, and Y. Kurobane (2009). *Design Guide for Rectangular Hollow Section (RHS) Joints under Predominantly Static Loading*. 2nd ed. Geneve: CIDECT.

Wardenier, J., G. J. van der Vegte, and D.K. Liu (2007a). "Chord stress function for rectangular hollow section X and T joints". In: *The 7th international Offshore and Polar Engineering Conference*, pp. 402–412.

Yu, Y. (1997). *The static strength of uniplanar and multiplanar connections in Rectangular Hollow Setions*. Delft: Delft University Press.

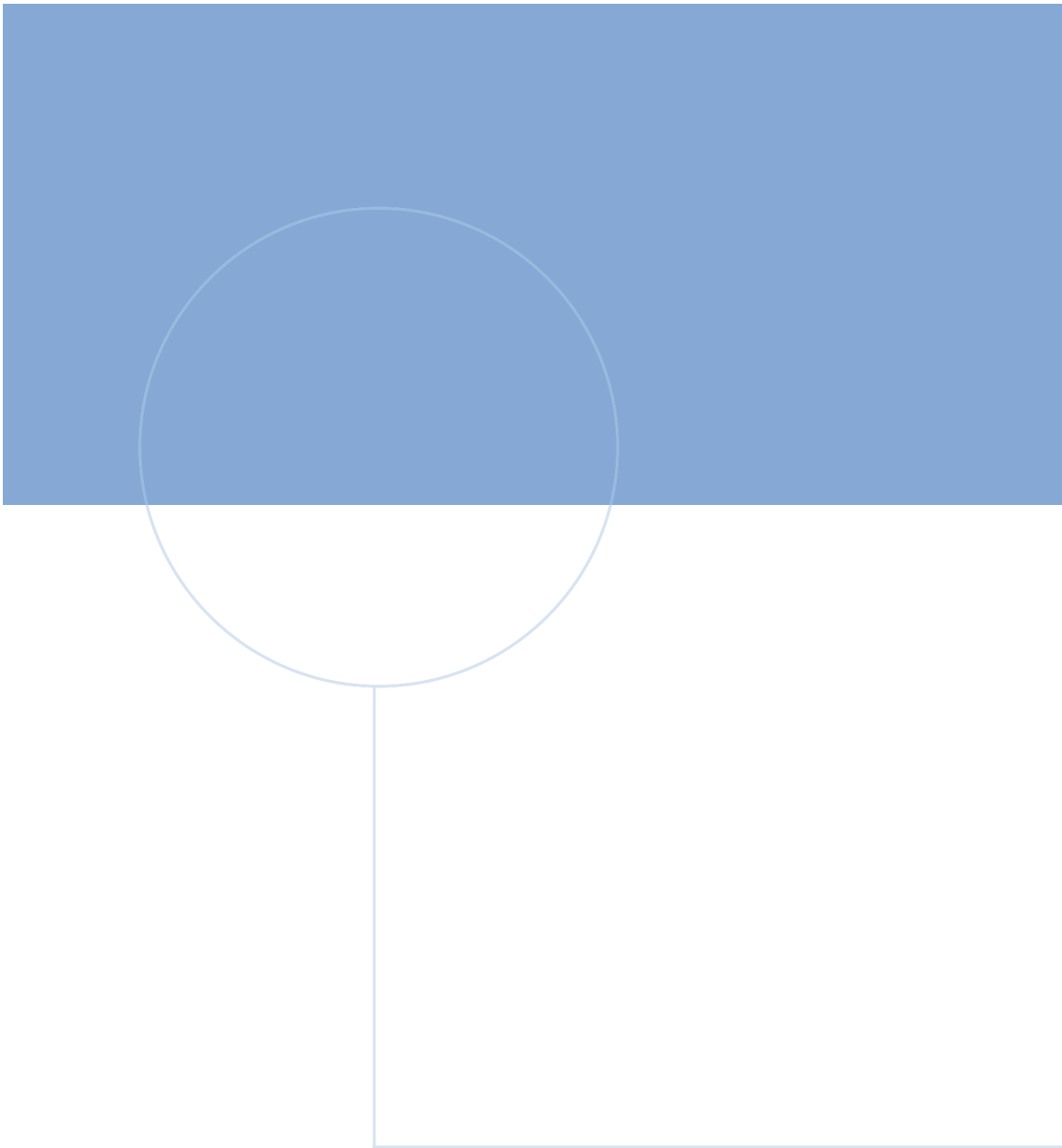

NTNU

Norwegian University of
Science and Technology